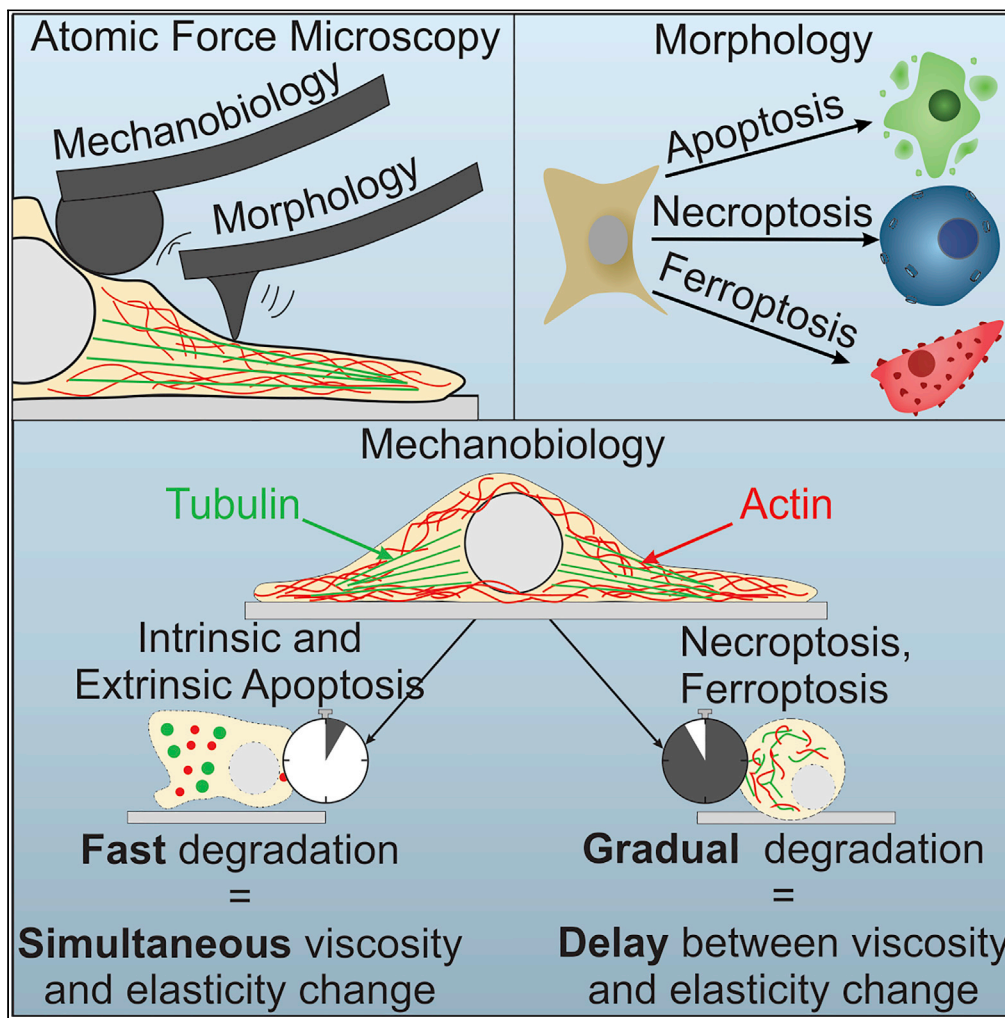## Article

AFM Analysis Enables Differentiation between Apoptosis, Necroptosis, and Ferroptosis in Murine Cancer Cells

Louis Van der Meeren, Joost Verduijn, Dmitri V. Krysko, André G. Skirtach

louis.vandermeeren@ugent.be

HIGHLIGHTS

AFM is a label-free method to distinguish apoptosis, necroptosis, and ferroptosis

Nanotopography and subtle morphologic changes are distinct for each RCD

Mechanobiology elasticity analysis reveals changes occurring at early stages of RCD

Microrheology data agree with mechanobiology Young's modulus analysis

Article

AFM Analysis Enables Differentiation between Apoptosis, Necroptosis, and Ferroptosis in Murine Cancer Cells

Louis Van der Meeren,[1,2,6,*] Joost Verduijn,[1,2] Dmitri V. Krysko,[2,3,4,5] and André G. Skirtach[1,2,5]

SUMMARY

Regulated cell death (RCD) has a fundamental role in development, pathology, and tissue homeostasis. In order to understand the RCD mechanisms, it is essential to follow these processes in real time. Here, atomic force microscopy (AFM) is applied to morphologically and mechanically characterize four RCD modalities (intrinsic and extrinsic apoptosis, necroptosis, and ferroptosis) in murine tumor cell lines. The nano-topographical analysis revealed a distinct surface morphology in case of necroptosis, $\sim$ 200 nm membrane disruptions are observed. Using mechanical measurements, it is possible to detect the early onset of RCD. Combined elasticity and microrheology analysis allowed for a clear distinction between apoptotic and regulated necrotic cell death. Finally, immunofluorescence analysis of the cytoskeleton structure during the RCD processes confirm the measured mechanical changes. The results of this study not only demonstrate the possibility of early real-time cell death detection but also reveal important differences in the cytoskeletal dynamics between multiple RCD modalities.

INTRODUCTION

Recent research revealed that regulated cell death (RCD) is omnipresent in various human pathologies and has applications in cancer therapy (Berthenet et al., 2020; Conrad et al., 2016; Friedmann Angeli et al., 2019). RCD is an umbrella term to cover the whole family of cell death modalities that are regulated by the intrinsic cell death program. During apoptosis, which is the most elaborately studied RCD modality, the internal components of the cell are dismantled, and disposed of, in apoptotic blebs (Figures 1A and 1B) (Tang et al., 2019). Apoptosis is very important in many biological processes including in cell infection by pathogens and also during development and normal tissue turnover (i.e., homeostasis). Apoptosis is an essential process since its evasion was shown to be one of the hallmarks of cancer (Hanahan and Weinberg, 2000). For a long time, necrosis was distinguished from apoptosis as a caspase-independent and accidental cell death modality. However, it was later discovered that in the presence of the correct stimuli, necrosis can be actively induced (Kaczmarek et al., 2013). To distinguish the accidental necrotic cell death (necrosis) from the actively induced necrotic cell death, the term necroptosis was introduced (Figure 1C). Subsequent research showed that several different pathways lead to RCD with necrotic morphology including ferroptosis (Figure 1D) (Friedmann Angeli et al., 2019; Galluzzi and Vitale, 2018). Ferroptosis, another regulated necrotic cell death, was discovered during a screening for molecules that can induce cell death in human foreskin fibroblasts. One of the tested molecules (erastin) induced a cell death that could not be prevented by the inhibition of apoptosis, necroptosis, and autophagy (Dixon et al., 2012). However, this novel cell death could be blocked by iron chelators.

Fluorescence microscopy and flow cytometry, the currently adopted standard to detect cell death in real time (Crowley et al., 2016; Demuynck et al., 2020), are based on the permeability of fluorescent dyes, or fluorophores, through the cell membrane. However, (1) fluorescent dyes potentially affect the process itself (i.e., phototoxicity) (Purschke et al., 2010), (2) fluorophores do not often allow discrimination between different cell death modalities (Krysko et al., 2008), and (3) current methods do not account for changes in mechanobiology, occurring during early stages of RCD modalities (Marx, 2019).

Atomic force microscopy (AFM, Supplemental note 1) is a nano-indenter technique that has recently gained substantial interest in the field of cell biology owing to its broad range of applications such as

[1]Nano-Biotechnology Laboratory, Department of Biotechnology, Faculty of Bioscience Engineering, Ghent University, 9000 Ghent, Belgium

[2]Cancer Research Institute Ghent, 9000 Ghent, Belgium

[3]Cell Death Investigation and Therapy Laboratory, Department of Human Structure and Repair, Faculty of Medicine and Health Sciences, Ghent University, 9000 Ghent, Belgium

[4]Department of Pathophysiology, Sechenov First Moscow State Medical University (Sechenov University), 119146 Moscow, Russian Federation

[5]Senior authors

[6]Lead Contact

*Correspondence: louis.vandermeeren@ugent.be

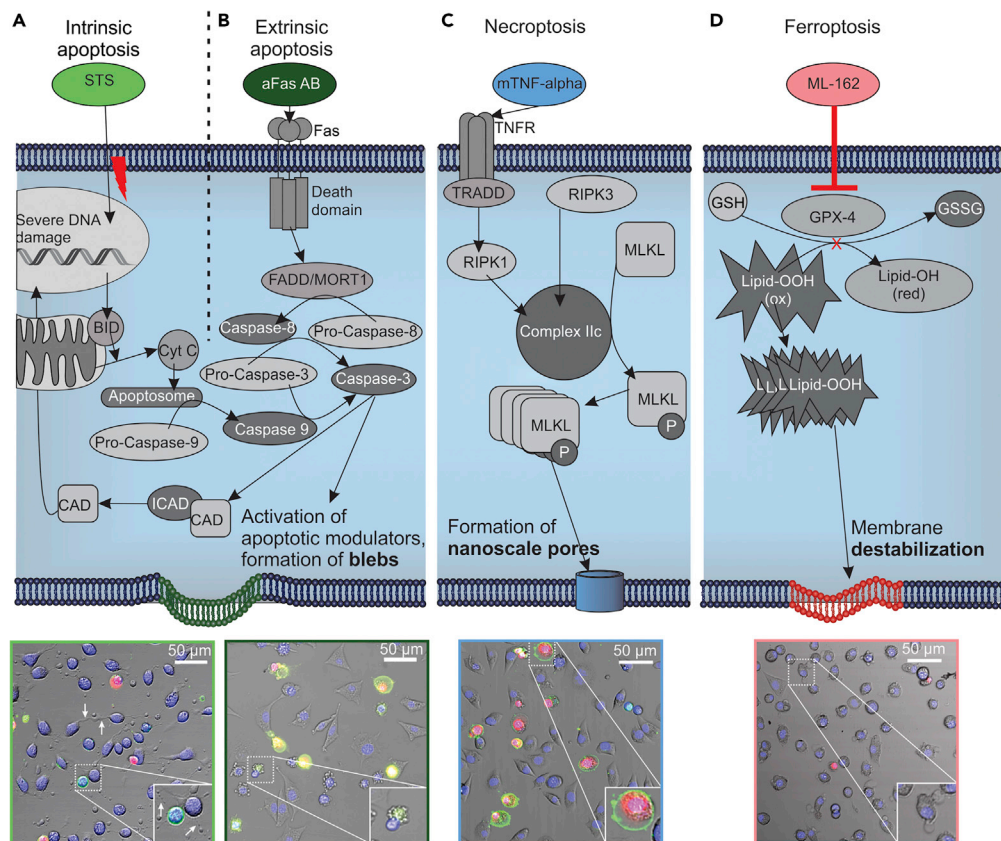https://doi.org/10.1016/j.isci.2020.101816

Figure 1. Schematic Overview of the Molecular Pathways of RCDs

(A–D) Schematic representation of the molecular pathways activated during intrinsic and extrinsic apoptosis, necroptosis, and ferroptosis, respectively. Below each modality, a confocal microscopical image is added to indicate the typical morphology for each cell death modality. (A) Strong cell shrinkage occurs during intrinsic apoptosis with remaining focal adhesion points (white arrows). (B) In extrinsic apoptosis, a strong shrinkage is accompanied by apoptotic blebbing. (C) Cellular swelling in necroptosis followed by detachment. (D) Cellular shrinkage in ferroptosis is followed by membrane integrity loss leading to membrane protrusions. The fluorescent markers used in the confocal experiments are AnnexinV-Alexa Fluor 488 (green, visualizing phosphatidylserine), Hoechst 33342 (blue, visualizing nuclei), Propidium iodide (red, visualizing nucleus post membrane permeabilization). Insets show an enlarged view of cells. Scale bar, 50 μm. See also Figure S1.

investigation of topographic imaging and mechanical properties (Dufrêne et al., 2017; Fernandes et al., 2010). This technique was previously used in RCD research, but existing research mainly focused on apoptosis. Morphological (Kim et al., 2012; Kwon et al., 2015; Liu et al., 2019; Su et al., 2019) and elasticity analysis (Nikolaev et al., 2014; Pelling et al., 2009) are the two main approaches used. The main contributors to cellular elasticity are the cytoskeletal compounds (actin, tubulin, and intermediate filaments) (Fletcher and Mullins, 2010). It was previously reported that during apoptotic cell death the cytoskeleton is actively degraded (Oropesa-Ávila et al., 2017; Pelling et al., 2009). However, to the best of our knowledge, no information exists on the fate of the cytoskeleton (and consequentially the cellular mechanical changes) during the process of other RCD modalities.

To test the differences between multiple RCD modalities a specialized L929 mouse fibrosarcoma cell line, transfected with the human Fas-receptor (Fas) to produce L929sAhFas, is used (Vanhaesebroeck et al., 1992; Vercammen et al., 1997). Intrinsic apoptosis is activated by different exogenous and endogenous stimuli converging on mitochondrial outer membrane permeabilization; exposing L929sAhFas cells to staurosporine (STS) results in cell death with an intrinsic apoptotic morphology (Figure 1A) (Belmokhtar et al., 2001; Hessler et al., 2005; Humphreys and Wilson, 1999). Extrinsic apoptosis ensues after the activation of plasma membrane receptors (Galluzzi et al., 2018). Owing to the expression of human Fas in the

cells, it is possible to induce extrinsic apoptosis by exposing the cells to anti-Fas antibody (aFas Ab). Upon binding of aFas Ab, the death-inducing signaling complex (DISC) is formed with FADD and procaspase-8, which leads to the caspase-8 activation and consequently execution phase of apoptosis (Figure 1B) (Belmokhtar et al., 2001; Elmore, 2007; Humphreys and Wilson, 1999). In contrast, necroptosis can be induced by exposing L929sAhFas cells to murine tumor necrosis factor (mTNF), binding of mTNF on its receptor results in the formation of complex IIc (through recruitment of RIPK1, RIPK3, and TRADD) and consequently MLKL phosphorylation and oligomerization (Figure 1C) (Kaczmarek et al., 2013; Silke and Brink, 2010; Vercammen et al., 1998). These oligomers form lipid destabilizing pores, eventually resulting in cell death (Dondelinger et al., 2014; Ros et al., 2017; Zhang et al., 2018). Ferroptosis can ensue after dysregulation of the lipid peroxide metabolism (Figure 1D). In L929sAhFas cells, ML162 inhibits glutathione peroxidase (GPX4), from which ferroptotic cell death is initiated owing to the accumulation of peroxidized lipids (Cao and Dixon, 2016).

Here, AFM is used to investigate the nano-topography and mechanics (Alsteens et al., 2017) of live cells undergoing four different RCD modalities (i.e., extrinsic and intrinsic apoptosis, necroptosis, and ferroptosis) in real time and in one cellular context. For all RCD modalities, specific morphological characteristics could be identified such as an increase in the surface roughness in the early stages of the process. Force measurements on cells undergoing different modes of RCD revealed a significant decrease of the cell elasticity compared with control cells, and these differences can be noticed before cells enter a late stage of RCD. Next, a microrheological analysis was performed on the cells during the RCD modalities. These data provide information on the internal viscoelastic state in the cell, which is seen to be more solid in living cells versus more fluid in dead cells for all RCD modalities. By comparing the dynamics in the microrheological data with the obtained elasticity data for each RCD modality, it is possible to make a clear distinction between apoptotic and regulated necrotic cell death (i.e., necroptosis and ferroptosis). Immunofluorescent staining of the major cytoskeleton components actin and tubulin confirms the data observed in the mechanical analysis based on the disaggregation and degradation of these cytoskeletal proteins during the process of RCD.

RESULTS

The Morphological Analysis Shows Distinctive Characteristics in Different RCD Modalities

After performing induction/inhibition experiments for the different RCDs in the L929sAhFas cell line (Figure S1), the cells were fixed at a certain time point after adding the respective inducers. Time points were chosen when the cell death process was already initiated but had not progressed to the state of cell detachment. In the performed experiments, cells were fixed 3 h post induction and imaged with AFM (Figure S2A). During intrinsic apoptosis, induced by STS, the whole cell shrinks leading to the formation of irregular structures (Figure 2A), but several focal adhesion points remain attached to the substrate (Figure 2A). These observations are similar to the previously reported results on the relocation of the cytoskeleton to protrusions and inhibition of blebbing by STS (Charras et al., 2005; Pelling et al., 2009). In extrinsic apoptosis, an increased shrinkage can be observed accompanied by numerous smaller apoptotic bodies (approximately 5 μm in diameter), which are shown in the height profiles (Figure 2B). In contrast, necroptotic cells do not shrink but detach and swell during the process of cell death (Figure 2C); small membrane disruptions or pores of varying diameters above 200 nm can be distinguished, which presumably originate from the insertion of MLKL oligomers in the cellular membrane (Moreno-Gonzalez et al., 2016); examples of the characteristic diameter and depth of these pores are shown on the height profiles (Figure 2C). It can be noted that these pores are similar in size to gasdermin pores, which were previously observed with AFM, in pyroptosis (Liu et al., 2019). During ferroptosis, it can be noticed that circular protrusions are formed on the membrane ranging from 1 to 5 μm, as it is indicated on the height profiles (Figures 2D and S2B). Most likely these irregularities originate from the destabilization of the membrane due to the accumulation of peroxidized lipids (Kagan et al., 2017; Tyurina et al., 2019).

An additional advantage of the AFM morphological imaging is that it allows for the extraction of quantitative 3D data on nano-topography, which can be used to distinguish between different cell states (Sokolov et al., 2018). In that regard, for all RCD modalities, the surface roughness (average roughness [Ra], root-mean-square roughness [Rq], and valley-to-peak roughness [Rt]) of cells undergoing these RCD modalities were analyzed. For each of these parameters, there is a significant increase of the roughness for each RCD compared with control (Figure 2E).
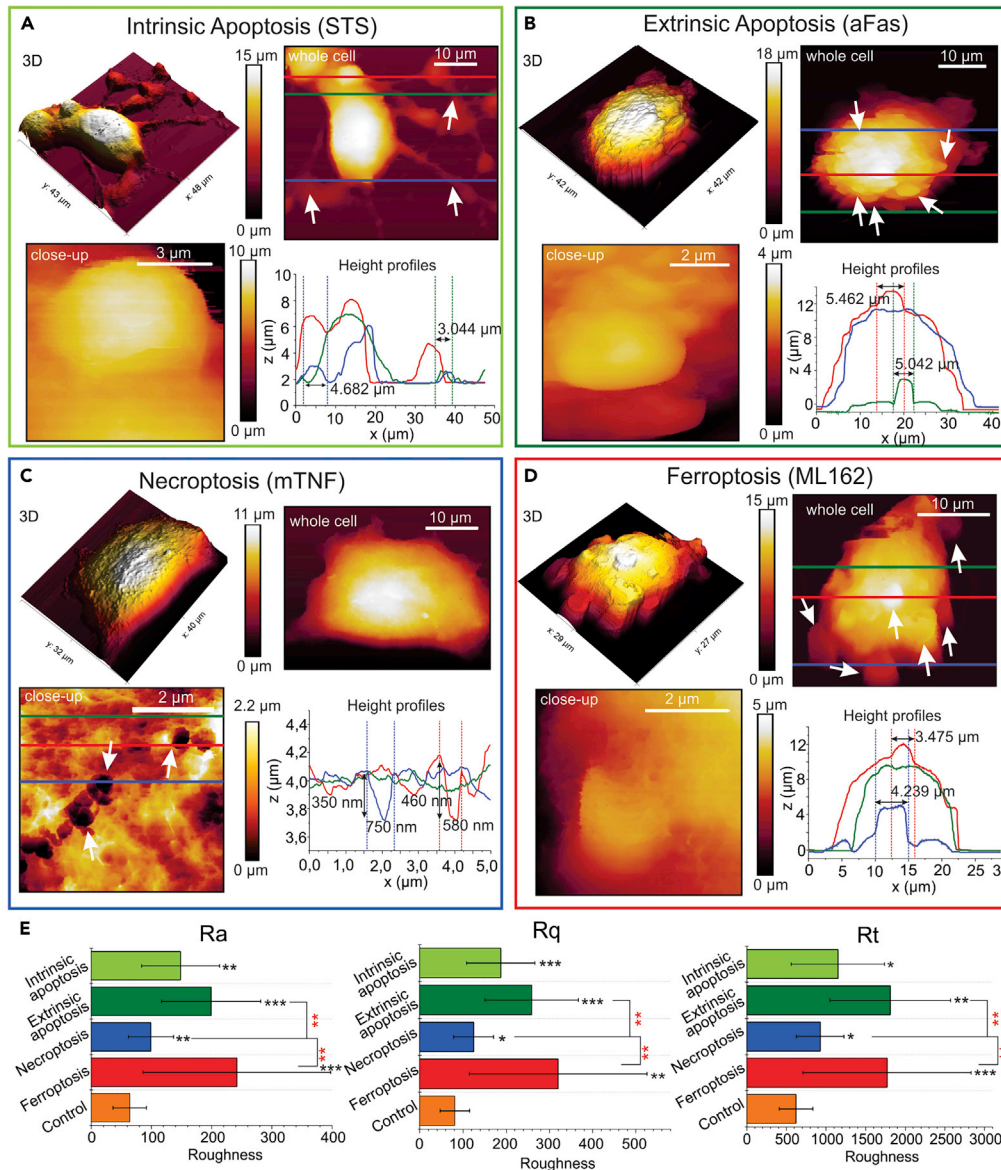
Figure 2. Morphologic Analysis of the Cellular Changes in the Early Stage of Cell Death by AFM

(A–D) Four-panel morphological characterization: top left, 3D AFM image; top right, whole-cell 2D AFM image; bottom left, AFM close up of RCD modality-specific characteristics; bottom right, profiles indicating geometries of typical characteristics noticed for each RCD. (A) Intrinsic apoptosis is characterized by shrinkage while maintaining adhesion points (white arrows), height profiles indicate diameters of the remaining focal adhesion points, close-up (bottom-left panel) shows observed surface irregularities in the intrinsic apoptosis. (B) Extrinsic apoptosis is characterized by total cell shrinkage and extensive blebbing (white arrows), height profiles: the average diameters of blebs. (C) Necroptosis is characterized by the overall shrinkage accompanied by the appearance of sub-micron pore-like membrane disruptions (white arrows in the close-up [bottom left panel]), height profiles: the diameter and depth of the pores. (D) Ferroptosis is characterized by the shrinkage and the presence of uniform circular membrane protrusions (indicated by white arrows), height profiles: dimensions of these protrusions.

(E) Bar graph comparing three roughness parameters extracted from AFM images: Ra, the average roughness; Rq, the RMS roughness; Rt, the maximum height of the profile. For all RCD modalities, a significant increase is noted (black stars) compared with control cells (orange bars), which allows to quantitatively distinguish dead cells from viable cells based on morphological data. Both ferroptotic and extrinsic apoptotic cells also exhibit a significantly higher roughness compared with that for necroptotic cells (red stars). Error bars represent the standard deviation (n = 15). The statistical analysis was determined by a Kruskal-Wallis test followed by a pairwise Wilcoxon test with Benjamini-Hochberg adjusted p values (*p < 0.05, **p < 0.01, ***p < 0.001). See also Figure S2.

In the final step of the morphological analysis, live cells were imaged with AFM to visualize the morphological dynamics during the RCD process (Figures S2C–S2E). Although this analysis was partly impeded by the detachment of cells during the RCD process, we can already notice from this analysis that the clear cross-linked net-like cytoskeleton structure, present in the early stages of cell death, disappears over time for all RCD modalities (Figures S2C–S2E). This strongly points out that during the cell death process mechanical changes occur since the cytoskeleton is the main contributor to cellular elasticity (Pegoraro et al., 2017). The following part of this work focuses on the mechanical changes of cells undergoing different RCD modalities.

Elasticity Changes Allow Early Detection of RCD Onset

Previously, research has shown that apoptotic cell death could be linked to a decrease in cellular elasticity (Nikolaev et al., 2014; Wu et al., 1998). Moreover, this decrease could be linked to the degradation of the cytoskeleton by combining AFM and confocal microscopy studies (Pelling et al., 2009). Although differences between the morphology of RCD modalities have been described extensively, such information does not exist about the mechanical changes during these processes (Galluzzi et al., 2018).

The measurements in this study are performed on the nucleus (Figure 3A, the blue area indicated by the probe), the area with the most uniform elasticity distribution, which allows avoiding artificial inflation of elasticity due to the underlying substrate. Importantly, the induction of RCD is simultaneously followed with fluorescence microscopy allowing one to confirm the end stage of cell death (indicated by membrane permeabilization, Figure S3A). Initially, the AFM setup was tested on control cells, in which elasticity was successfully analyzed for up to 7 h (Figure S3B). During this control experiment, the elasticity of the cells remained unchanged after a small initial increase. Moreover, no cell death was observed during the time span of the control experiment. The dynamics of the cellular elasticity were analyzed for each RCD modality by following 50 cells (in total) over three independent experiments (Figures 3C–3F). During intrinsic apoptosis a rapid decrease of mechanical strength can be noticed from 1,300 to 400 Pa at 15 min post induction, which remains steady after the initial drop (Figure 3C), also confirming the previously reported data (Pelling et al., 2009). In contrast, an increase in elasticity from 1,200 to 1,400 Pa is observed during extrinsic apoptosis at 60 min post induction preceding the fast drop to 500 Pa (Figure 3D). Owing to the externalization of phosphatidylserine during the early stages of apoptosis, Annexin V-linked probes can be used to detect early stages in apoptotic cell death (Segawa and Nagata, 2015). The addition of Annexin V-Alexa Fluor™ 488 to the AFM experiments allowed analyzing how this early cell death marker compares with the detected mechanical changes (Figures S3D and S3E). For intrinsic apoptosis (induced by STS), it can be noticed that mechanically the cells already approximately reached their final elasticity stage, whereas no Annexin V (AnnV) or PI staining is yet visible. During extrinsic apoptosis, the increase in the number of cells with AnnV labeling concurs with the significant decrease in elasticity. What is particularly interesting in the case of extrinsic apoptosis is that the increase in elasticity precedes the increase in the number of AnnV$^+$ cells. This underlines an additional advantage of mechanical measurements of the state of cells, thus allowing detection of any variation.

Finally, for necroptosis and ferroptosis, the elasticity constantly decreases from around 1,000 Pa initially to 182 and 210 Pa, respectively, over the 5h course of the experiment (Figures 3E and 3F). Overall, our data show a significant reduction of the elasticity from 1,100 Pa toward 200 Pa in all RCD modalities after the membrane permeabilization (as measured by PI$^+$). This decrease in elasticity is significantly different in comparison with viable cells for each RCD modality before any fluorescence (PI$^+$) signal can be detected in these cells. These two events are separated by 116, 40, 33, and 129 min for intrinsic apoptosis, extrinsic apoptosis, necroptosis, and ferroptosis, respectively (Figures 3C–3F, rectangles shaded with corresponding colors and Table S1). These data show that, with AFM, it is possible to detect the earlier stages of cell death purely based on the elasticity changes and before any signs that the membrane permeabilization occurs (PI$^+$).

Interestingly, when comparing the dynamics of the elasticity of different RCD modalities with each other, the data indicate that the rate of the elasticity decrease is faster in apoptotic cell death (intrinsic and extrinsic) compared with regulated necrotic cell death (necroptosis and ferroptosis). To quantify this observation, the first-order derivative of the elasticity change over time is taken, to obtain the rate of elasticity decrease during the process of RCD (Figure S3C, Table S2). Interestingly, a dichotomy can be observed between a significantly faster decrease rate in apoptotic RCD (maximum decrease of −42.27 and −16.21 Pa/min for intrinsic and extrinsic apoptosis, respectively) compared with a more steady decrease in necrotic
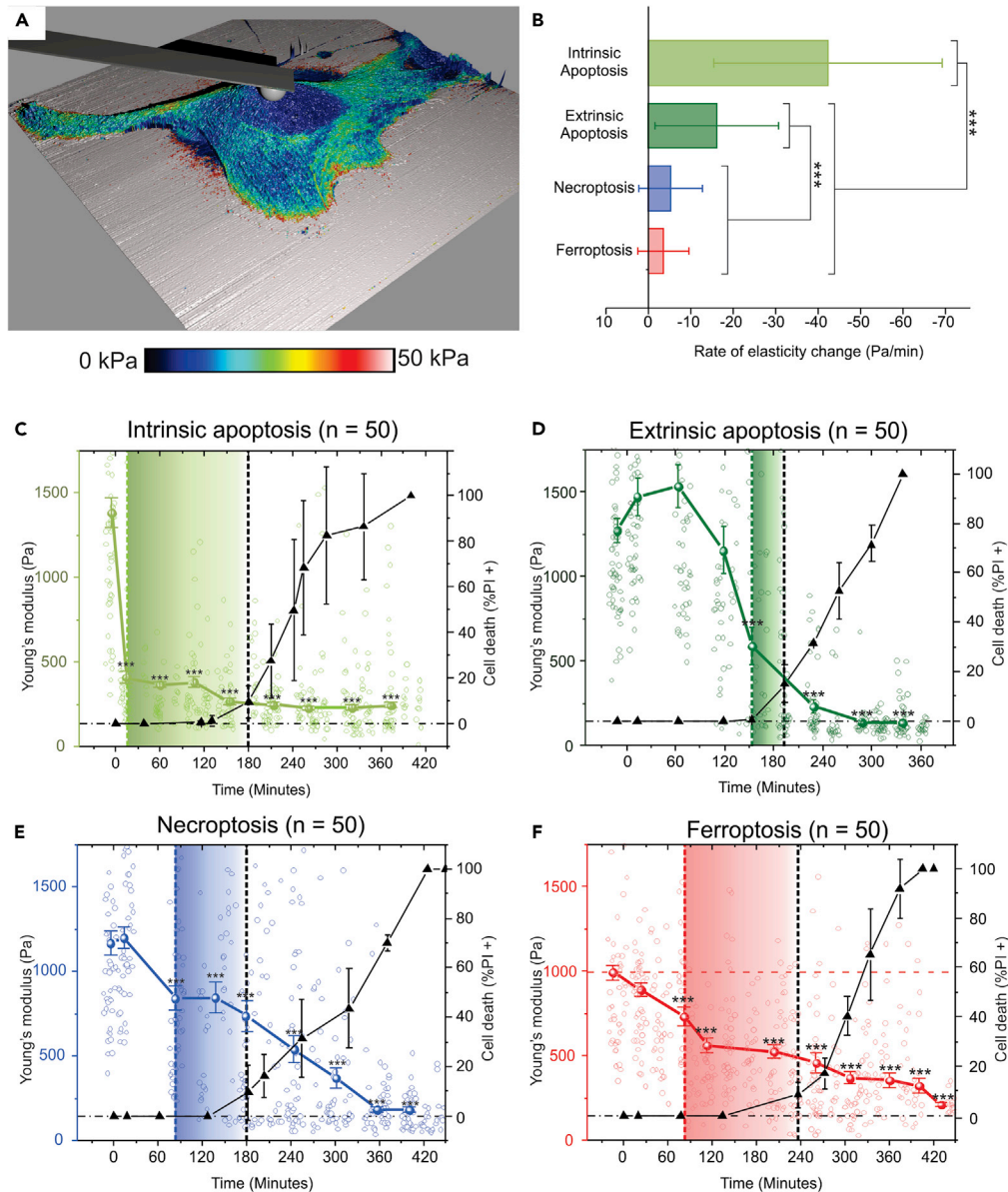
Figure 3. AFM Mechano-Biology Analysis of the Elasticity Dynamics of Cells Undergoing RCD Modalities

(A) A single-cell high-resolution elasticity analysis indicating the uniform elasticity distribution in the nuclear area (i.e., the blue area indicated by the cantilever immobilized spherical colloidal probe).

(B) Bar graph indicating the maximum decrease rates during the process of each RCD modality. For both intrinsic and extrinsic apoptosis, a significantly higher decrease rate is observed compared with the other modalities (p values are provided in Table S2). The error bars in the right y axis of the graph indicate the standard deviation.

(C–F) The time dependence of the elasticity of cells undergoing intrinsic apoptotic, extrinsic apoptotic, necroptotic, and ferroptotic RCDs, respectively: left y axis and the colored line indicate elasticity values, right y axis and black line indicate a late stage of cell death determined by the PI status (expressed as the percentage of the measured cells), shaded rectangles indicate the delay between the first significant difference in elasticity compared with the first cell death signal (PI$^+$). (C) Intrinsic apoptosis is characterized by a steep elasticity drop at the frist timepoint of measuring, detection with fluoresence lags behind significantly (166 minutes). (D) Extrinsic apoptosis shows an initial elasticity increase which is followed by a steep elasticity decrease, first detection with fluoresence lags behind 40 minutes. (E) Elasticity decreases gradually during necroptosis, a significant decrease of elasticty can be discerned 99 minutes before the first fluorescent signal appears. (F) Ferroptosis is characterized by a gradual elasticity decrease over time of the cell death process, significant elasticity decrease precedes the fluorescent signal by 155 minutes. The error

Figure 3. *Continued*
bars in the left y axis graphs indicate the standard error of means (SEM) n = 50. Errorbars for the data on the right y-axis represent the standard deviation. (The statistical analysis was determined by a Kruskal-Wallis test followed by a pairwise Wilcoxon test with Benjamini-Hochberg adjusted p values, ***p < 0.001; n = 50). See also Figure S3 and Tables S1–S3.

RCD (maximum decrease rate of −5.13 and −3.57 Pa/min for necroptosis and ferroptosis, respectively) (Figure 3B and Table S3).

Proving that described above AFM measurements are cell-line independent, similar experiments were performed for the most recently discovered RCD modality, namely, ferroptosis, in murine fibrosarcoma MCA205 cells (Figures S3D and S3E). In this case, a significant decrease of elasticity was be detected 69 min post induction (n = 20). Furthermore, during ferroptosis, the elasticity drastically decreased from 1,000 to 116 Pa. These experiments show similar results to those observed for ferroptotic L929sAhFas cells.

Microrheological Changes during the RCD Allows Differentiation between Apoptotic and Regulated Necrotic Cell Death

Cells, however, do not behave like perfectly elastic objects suggesting to probe their viscoelastic properties. AFM allows investigating the viscoelastic status of cells by performing microrheology measurements (Figure 4A) (Alcaraz et al., 2003; Weber et al., 2019). This information is obtained by analyzing the mechanical reaction of cells toward oscillating indentation forces at increasing frequencies. Such analysis is particularly interesting for cells since it allows linking the solid-liquid state of cells with the state of the cytoskeleton. When analyzing the shear storage (G′) and shear loss (G″) of cells at increasing frequencies of oscillations, a power-law behavior can be observed (Figures 4B and S4A, Supplemental note 2. A physical interpretation of this behavior was suggested by Fabry et al. (2001), who has proposed a model pointing out that cells can be seen as a specific case of soft glassy rheology (SGR) (Figure S3C) (Sollich et al., 1997). Fitting the observed values for both G′ and G″ to this model showed a high correlation (Figure 4B, $R^2 > 0.97$), and that supports the use of the interpretation of this model in the subsequent microrheological analysis.

In this SGR model, the loss tangent, defined as the ratio of G′′ (oscillation energy lost) over G′ (oscillation energy stored), translates to a measure, which is probe independent, of the solid-like (loss tangent <1) versus fluid-like behavior (loss tangent >1) of the internal structure. Similarly to Young's modulus (elasticity) analysis, the dynamics of the loss tangent (viscoelasticity) are also analyzed for each RCD modality (Figures 4C–4F). Furthermore, a distinct feature of our analysis is the comparison of the dynamics of the microrheological analysis to that of the elasticity changes of cells for each RCD. When comparing the time-dependent dynamics of the microrheology with the elasticity data, again a clear separation can be made between the apoptotic and the regulated necrotic cell death modalities. In apoptotic cell death, the significant increase of the loss tangent coincides with the significant drop of the elasticity, whereas in necroptosis and ferroptosis these events are separated by 176 and 172 min, respectively (indicated in Figures 4C–4F by colored rectangles, Table S4).

Analysis of Actin and Tubulin Dynamics during RCD Provides Interpretation for Mechanical Changes

Our previous data show that cellular elasticity decreases and fluid behavior increases during all RCD modalities; most likely, these changes are caused by changes in the cytoskeletal proteins (CSP) organization. To test this hypothesis, two major components of the cytoskeleton were analyzed using immunofluorescence, namely, actin and alpha-tubulin. It is known that these two proteins are the main contributors to mechanical strength in cells (Pegoraro et al., 2017; Xia et al., 2019). Besides control L929sAhFas cells (Figure 5A), L929sAhFas cells were also fixed during the process of different RCD modalities at time points when mechanical dynamics differed most in between the different modalities (Figures 5B–5D, left, black arrows).

In control cells, both of these proteins show a strongly cross-linked structure of fibrils (Figure 5A). The actin presence is the most visible at the cellular membrane (often referred to as actin cortex) (Chugh and Paluch, 2018), whereas tubulin is more pronounced in the cytosol regions. The DNA content has been marked, which shows that the nucleus in control cells is delineated and has a circular form.
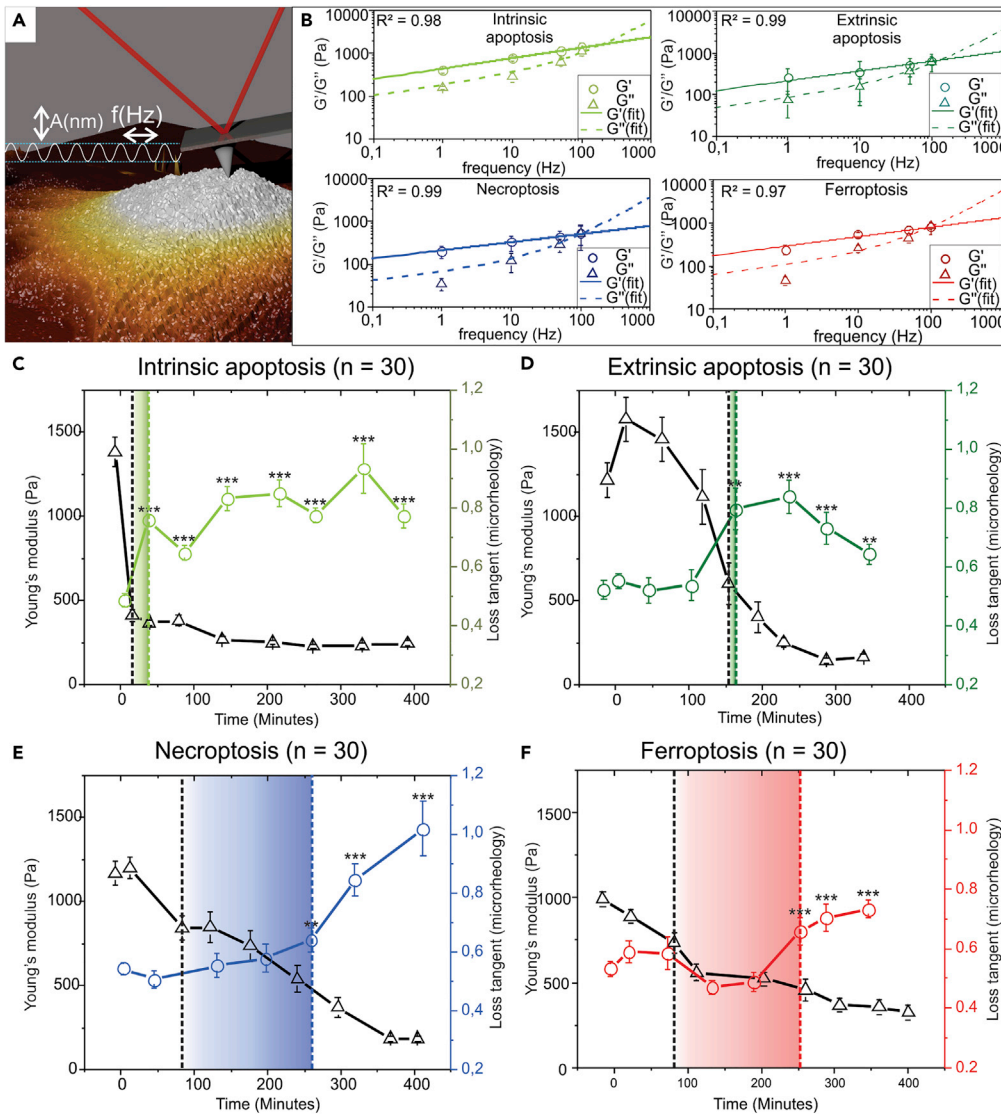
Figure 4. Side-by-Side Analysis of Microrheological Changes and Elasticity Dynamics

(A) Schematic representation of a microrheological oscillation measurement allowing measurement of viscoelastic properties of soft materials, with A (nm) indicating amplitude and f (Hz) frequency.

(B) Fit of soft glassy rheology (SGR) model over the frequency range 0.1–100 Hz for late stages of intrinsic and extrinsic apoptotic and necroptotic and ferroptotic cells showing the response of the cells shear storage and shear loss to increasing modulation frequencies. R^2 values at the top left of each plot show the correlation coefficient of the shear data (G′ and G″) with the SGR model.

(C–F) Pairwise comparison of elasticity versus dynamic in cellular microrheology (represented by a loss tangent). The shaded squares indicate the point from which a significant difference, in comparison with the control, in either Young's modulus or the loss tangent can be noticed. (C) During Intrinsic apoptosis the loss tangent increases quickly after induction simultaneously with the change in elasticity. (D) In extrinsic apoptosis a simultaneous fast increase in loss tangent and elasticity decrease can be noticed which occurs after the short elasticity increase. (E) Loss tangent change in necroptosis is gradual and lags behind the significant change in elasticity (176 minutes). (F) During ferroptosis the loss tangent increase is gradual and lags behind the significant elasticity decrease (172 minutes). The error bars in the loss tangent graphs indicate the standard error of means (SEM) n = 30 (statistical significance is compared with control cells, calculated with a Wilcoxon rank-sum test: **p < 0.01, ***p < 0.001). (C° See also Figure S4 and Table S4.

In intrinsic apoptosis, as induced by STS, starting from the first hour after the induction most of the fibril structures of the cytoskeletal proteins (CSP) have already disappeared (Figure 5B). Only actin fibers in the focal adhesion points remain. During later time points, the cell continues to shrink, and the focal
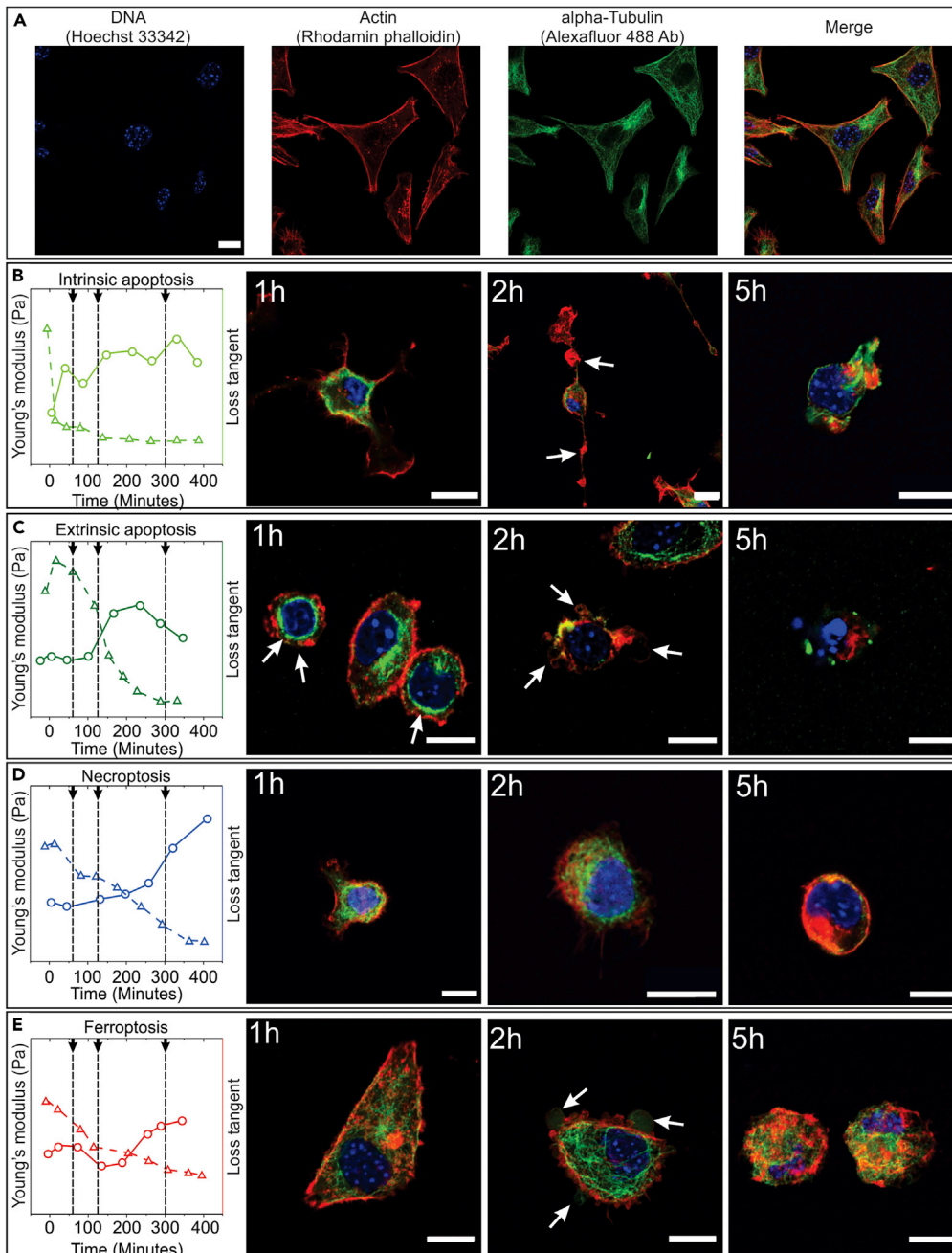
Figure 5. Cytoskeleton Dynamics during RCD Analyzed by Actin and Alpha-Tubulin Immunofluorescence

(A) Structure of control L929sAhFAS cells, the DNA content is stained with Hoechst 33342 (blue), actin is stained with Rhodamine Phalloidin (red), and Alpha-Tubulin is stained with Alexa Fluor 488 antibody (green) (scale bar, 10 μm).

(B–E) Series of four panels for each RCD modality showing the changes in the cytoskeleton during the RCD process. Left to right: a schematic of the measured mechanical changes, elasticity changes indicated by a dotted line and triangles, microrheological changes indicated by full line and circles. Black arrows pointing to dashed lines: time points at which the state of the cytoskeleton was analyzed, followed by confocal images at these respective time points (scale bar, 10 μm). (B) Intrinsic apoptosis: cellular shrinkage with typical long remaining focal adhesion points containing irregularities (white arrows), fast cytoskeleton degradation. (C) Intrinsic apoptosis: cellular shrinkage followed by blebbing (white arrows), a short period of concentration of cytoskeleton near the nucleus is followed by rapid degradation. (D) Necroptosis is characterized by overall rounding of the cell; cytoskeletal structure remains intact during earlier time points. (E) In ferroptosis, the cytoskeleton remains intact during earlier time points, membrane blebs can be distinguished (white arrows).

adhesion points remain, and at 5 h post induction cells start to detach. At this point, any fibril structure in both actin or tubulin has been lost forming randomly oriented and distinguished clumps of CSPs. Some clear differences can be distinguished in extrinsically induced apoptosis. Although cells also shrink, no focal adhesion points remain as observed in intrinsic apoptosis (Figure 5C). Moreover, one can see accumulations of both actin and tubulin surrounding the nucleus (Figure 5C and 1 h), which correspond to a small increase in mechanical strength at the early stages of apoptosis and which agrees with previously published data (Oropesa-Ávila et al., 2017; Pelling et al., 2009). In the next stage of extrinsic apoptosis, one can distinguish the presence of actin in the apoptotic blebs (Figure 5C and 2 h), but the overall structure of cross-linked fibers is lost. This degradation of actin and tubulin is in line with what was seen in the concurrent decrease of Young's modulus and an increase of the loss tangent. In the final stages of apoptosis, a complete condensation and breakdown of the nucleus can also be noticed.

In contrast to apoptosis, necroptosis and ferroptosis show different dynamics (Figures 5D and 5E). During these cell death modalities, a more gradual decrease of elasticity can be noticed in the AFM analysis. In necroptosis cells round up during the initial time points (Figure 5D and 1 and 2 h). However, a clear cross-linked fibrillar structure (mainly of tubulin) can still be distinguished. These cross-linked structures disappear only at the late stage (Figure 5D and 5 h). We suggest that the initial drop of Young's modulus corresponds to the loss of a strong attachment and a loss of the cross-linking between the compounds of the cytoskeleton leading to a rounding up of the necroptotic cell, whereas the delayed increase of loss tangent (and a further decrease of Young's modulus) corresponds to the moment when all cytoskeleton components are disassociated. In ferroptosis, the same trend can be distinguished (Figure 5E), albeit with one clear difference: at 2 h post induction, clear membrane protrusions (Figure 5E and 2 h) can be distinguished. Interestingly, these big membrane protrusions differ from apoptotic blebs (Figure 5C and 2 h) in the fact that they are not surrounded by a layer of actin.

DISCUSSION

In this work, four different regulated cell death (RCD) modalities were characterized using a label-free microscopy technique, AFM. This technique allows to analyze the morphological and mechanical characteristics of single cells with high sensitivity. The goal of this work is to analyze how AFM can be used to characterize and potentially differentiate between RCD modalities.

In the nano-topographical analysis of the cellular morphology, clear morphological characteristics are observed for each of the cell death modalities. To quantify these morphological changes the roughness values can be analyzed. For each of the analyzed parameters, a significant increase was noted compared with control cells. The smallest increase is reported for necroptosis, attributable to the nanoscale pore-like structures (Figure 2C). For intrinsic apoptosis, the increase of roughness is caused by the fast shrinkage leading to the occurrence of irregular structures (Figure 2A). For both extrinsic apoptosis and ferroptosis a significant increase for Ra, Rq, and Rt is measured compared with both control cells and necroptotic cells (Figure 2E). These big increases in surface roughness can be explained by the presence of numerous apoptotic bodies (in extrinsic apoptosis) (Figure 2B) or membrane destabilization (in ferroptosis, Figure 2D).

Following the morphologic analysis, a thorough mechanical characterization was performed on each of the RCD modalities. Analysis of the elasticity changes during the process of each RCD modality showed that a significant decrease of elasticity consistently preceded fluorescent signal (which indicated membrane permeabilization, PI$^+$). From this, it can be concluded that elasticity analysis allows detection of cell death in an early stage (before reaching the end stage caused by membrane permeabilization), without the use of fluorescent probes which potentially affect the RCD process. Furthermore, when comparing the elasticity dynamics in different modes of RCD, clear differences could be distinguished (Figure 3B). Most likely the fast decrease in elasticity of cells undergoing apoptosis can be explained through an active reorganization and depolymerization of the cytoskeleton by protein activation/inhibition during apoptosis (such as MLCK, ROCKs, executioner caspases), as was previously shown (Doncel et al., 2017; Oropesa-Ávila et al., 2017). In this work, it has been suggested that, owing to the absence of any active reorganization in both necroptosis and ferroptosis, the elasticity decrease is more gradual. The decrease can be most likely explained by the overall decomposition of cellular components in the late stages of cell death. Intrinsic and extrinsic apoptosis also show a significant difference in decrease rate between each other. It was previously reported that, depending on the time of caspase activation, two different apoptotic morphologies can be distinguished with distinctive cytoskeleton reorganization and breakdown dynamics (Oropesa-Ávila et al., 2017). This reorganization of the cytoskeleton, into a contractile actin-

myosin ring, is needed to enable the cell to synthesize the apoptotic bodies efficiently; since STS is known to inhibit apoptotic body synthesis, a reorganization step is likely skipped and cytoskeleton degradation ensues immediately resulting in an increased elasticity decrease rate (Charras et al., 2005). Moreover, in extrinsic apoptosis an increase in elasticity is noticed before the eventual decrease; this increase is most likely caused by the contraction of the actin-myosin ring.

In a microrheological analysis, it is possible to characterize the changes in viscoelastic properties (portrayed by the loss tangent) of the cells during the RCD process. These data showed that, for each RCD modality, a significant increase in liquid-like behavior could be distinguished. By putting the viscoelastic dynamics side to side with the previously acquired elasticity data it was possible to make a clear distinction between coinciding fast elasticity decrease and loss tangent increase in apoptotic cell death versus a delay between gradual elasticity decrease and loss tangent increase in the regulated necrosis cell death modalities (necroptosis and ferroptosis) (Figures 4C–4F). It is conceivable that these quick changes in apoptosis are caused by an active reorganization and/or degradation of the cytoskeleton, consistent with previously reported data (Oropesa-Ávila et al., 2017). The observed delay between Young's modulus decrease and loss tangent increase in necroptosis and ferroptosis suggests that cytoskeleton degradation is more gradual. A possible interpretation of these data is that an initial loss of connection between cytoskeleton polymers decreases the elasticity, but it has only a small effect on the viscoelasticity. Only when the polymer chains are also degraded into oligomers, the fluid-like behavior of the cells will be dramatically affected resulting in a significant increase of the loss tangent.

In the last step of this research, all mechanical data were analyzed jointly with an immunofluorescence analysis visualizing two major components of the cytoskeleton (i.e., F-actin and alpha-tubulin). In intrinsic apoptosis, an almost instant loss of the cross-linked structure of fibrils in the cytoskeleton is observed. This supports the hypothesis that the rapid decrease of Young's modulus (elasticity) and the concurrent increase in the loss tangent (microrheology) in the early time points of cell death induction are caused by an active degradation of the cytoskeleton. During extrinsic apoptosis, an increase in elasticity is measured while the loss tangent remains stable. This is likely caused by the reorganization of the cytoskeleton. Although the elasticity can be affected by a reorganization, the microrheology reflects more the intactness of the cytoskeleton. Therefore, when the cytoskeletal compounds reorganize around the nucleus but the polymers remain intact, an increase in elasticity is noticed but the loss tangent is unchanged (Figure 5C). However, at the time point when the cytoskeletal polymers are degraded, (Figure 5C) a clear joined increase in loss tangent, and decrease in elasticity is noticed. This idea is supported by a paper in which researchers showed that cytoskeleton disrupting drugs (e.g., blebbistatin and latrunculin-A) led to an increase in loss tangent, whereas using a cross-link disturbing drug (CK666, changes actin network from a mesh-like structure to parallel arrangement) led to a significant decrease in elasticity but had no observable effect on the loss tangent (Rigato et al., 2017). During intrinsic apoptosis, no such delay can be observed between the elasticity and the microrheological changes. When analyzing the immunofluorescence images (Figures 5B and 1 h) it can be noticed that no reorganization occurs but that the cytoskeleton is immediately degraded, which supports this idea. Similarly, the delay between the changes in elasticity and microrheology in both necroptosis and ferroptosis can be explained by the same rationale as mentioned above. Although the elasticity starts to decrease as the cells detach (Figures 5D and 5E; 2 h), the loss tangent remains stable. Only at later time points, when the cytoskeleton has completely deteriorated (Figures 5D and 5E; 5 h), the loss tangent increases significantly. From these observations, it can be concluded that the elasticity serves as a sensitive parameter for changes in the organization of the cytoskeleton, whereas the viscoelasticity represents a more robust parameter for the intactness of the cytoskeleton.

In summary, AFM is revealed as a powerful, label-free technique to investigate cell death modalities. A morphological analysis allows observation of distinct characteristics for each RCD modality, specifically a significant increase of the membrane roughness compared with that for control cells. By performing mechanobiology and (visco-)elasticity analysis, it is possible to both detect the early onset of cell death, indicated by an elasticity decrease, and differentiate between apoptotic and regulated necrotic cell death modalities (based on the delay between elastic and visco-elastic dynamics). The analyses performed here provide additional insights into RCD thus paving the way to a better understanding of cytoskeletal dynamics during RCD. The mechanical data accumulated in this work prove to be an ideal basis for (1) further development and calibration of high-speed deformability cytometry instruments (Nawaz et al., 2020) and (2) label-free determination of cell death types in mixed populations.

Limitations of the Study

During the morphological AFM analysis, cells had to be fixed at specific time points; this fixation process potentially alters some morphological characteristics of the cells. Experiments were also performed on non-fixed cells; however; owing to the nature of cell death process that leads to detachment of the adherent cells the data of these experiments were of much lower quality. To improve on this in the future new protocols should be established which would allow holding cells in place preventing them from moving during the morphological measurements.

Although AFM allows for a very high sensitivity mechanical analysis, the throughput of this technique is low (100 cells/minute). If these data were to have any practical applications (i.e., drug testing), a higher-throughput method should be used. Examples of such technologies are now emerging, with the most promising being a distinct form of microfluidics (Nawaz et al., 2020). This, however, does not diminish the value of our results, since the highly sensitive data from the AFM can be used to define experiments and optimize calibration for such new techniques.

Finally, experiments in this work were performed in a murine cell model, specifically selected to induce and compare different cell death modalities in one cellular context. We are aware that there are some differences between murine cells and human cells. It is important in future research to analyze how these observations translate to human. Results of this work are seen to play an important role for development of new cell-based therapy approaches (Efimova et al., 2020).

Resource Availability

Lead Contact

Further requests and information for resources should be directed to and will be fulfilled by the lead contact, Louis Van der Meeren (louis.vandermeeren@ugent.be).

Materials Availability

No new reagents or materials were generated during this study.

Data and Code Availability

The raw data acquired during this work are available on Mendeley data: https://doi.org/10.17632/jm6yz5vzs8.1.

METHODS

All methods can be found in the accompanying Transparent Methods supplemental file.

SUPPLEMENTAL INFORMATION

Supplemental Information can be found online at https://doi.org/10.1016/j.isci.2020.101816.

AUTHOR CONTRIBUTIONS

Conceptualization: A.G.S., D.V.K, J.V., L.V.d.M.; Methodology: L.V.d.M.; Data collection: L.V.d.M.; Data Analysis-Writing initial draft: L.V.d.M.; Review and editing: L.V.d.M., J.V., A.G.S., D.V.K.; Supervision: A.G.S., D.V.K.

DECLARATION OF INTERESTS

The authors declare no competing interests.

REFERENCES

Alcaraz, J., Buscemi, L., Grabulosa, M., Trepat, X., Fabry, B., Farré, R., and Navajas, D. (2003). Microrheology of human lung epithelial cells measured by atomic force microscopy. Biophys. J. 84, 2071–2079.

Alsteens, D., Newton, R., Schubert, R., Martinez-Martin, D., Delguste, M., Roska, B., and Müller, D.J. (2017). Nanomechanical mapping of first binding steps of a virus to animal cells. Nat. Nanotechnol. 12, 177–183.

Belmokhtar, C.A., Hillion, J., and Ségal-Bendirdjian, E. (2001). Staurosporine induces apoptosis through both caspase-dependent and caspase-independent mechanisms. Oncogene 20, 3354–3362.

Berthenet, K., Castillo Ferrer, C., Fanfone, D., Popgeorgiev, N., Neves, D., Bertolino, P., Gibert, B., Hernandez-Vargas, H., and Ichim, G. (2020). Failed apoptosis enhances melanoma cancer cell aggressiveness. Cell Rep. 31, 107731.

Cao, J.Y., and Dixon, S.J. (2016). Mechanisms of ferroptosis. Cell. Mol. Life Sci. 73, 2195–2209.

Charras, G.T., Yarrow, J.C., Horton, M.A., Mahadevan, L., and Mitchison, T.J. (2005). Non-equilibration of hydrostatic pressure in blebbing cells. Nature 435, 365–369.

Chugh, P., and Paluch, E.K. (2018). The actin cortex at a glance. J. Cell Sci. 131, jcs186254.

Conrad, M., Angeli, J.P.F., Vandenabeele, P., and Stockwell, B.R. (2016). Regulated necrosis: disease relevance and therapeutic opportunities. Nat. Rev. Drug Discov. 15, 348–366.

Crowley, L.C., Marfell, B.J., Scott, A.P., and Waterhouse, N.J. (2016). Quantitation of apoptosis and necrosis by annexin V binding, propidium iodide uptake, and flow cytometry. Cold Spring Harb. Protoc. 2016, 953–957.

Demuynck, R., Efimova, I., Lin, A., Declercq, H., and Krysko, D.V. (2020). A 3D cell death assay to quantitatively determine ferroptosis in spheroids. Cell 9, 703.

Dixon, S.J., Lemberg, K.M., Lamprecht, M.R., Skouta, R., Zaitsev, E.M., Gleason, C.E., Patel, D.N., Bauer, A.J., Cantley, A.M., Yang, W.S., et al. (2012). Ferroptosis: an iron-dependent form of nonapoptotic cell death. Cell 149, 1060–1072.

Doncel, J.P., Ojeda, P.de la C., OropesaÁvila, M., Paz, M.V., Lavera, I. De, Mata, M.D. La, Córdoba, M.Á., Hidalgo, R.L., Rivero, J.M.S., Cotán, D., et al. (2017). Cytoskeleton rearrangements during the execution phase of apoptosis. In Cytoskeleton - Structure, Dynamics, Function and Disease, J.C. Jimenez-Lopez, ed. (InTech), pp. 151–169.

Dondelinger, Y., Declercq, W., Montessuit, S., Roelandt, R., Goncalves, A., Bruggeman, I., Hulpiau, P., Weber, K., Sehon, C.A., Marquis, R.W., et al. (2014). MLKL compromises plasma membrane integrity by binding to phosphatidylinositol phosphates. Cell Rep. 7, 971–981.

Dufrêne, Y.F., Ando, T., Garcia, R., Alsteens, D., Martinez-Martin, D., Engel, A., Gerber, C., and Müller, D.J. (2017). Imaging modes of atomic force microscopy for application in molecular and cell biology. Nat. Nanotechnol. 12, 295–307.

Efimova, Iuliia, Catanzaro, Elena, Van der Meeren, Louis, Turubanova, Victoria D., Hammad, Hamida, Mischenko, Tatiana A., Vedunova, Maria V., Fimognari, Carmela, Bachert, Claus, Coppieters, Frauke, Lefever, Steve, Skirtach, Andre G., Krysko, Olga, and Krysko, Dmitri V. (2020). Vaccination with early ferroptotic cancer cells induces efficient antitumor immunity. J. Immunother. Cancer 8, e001369.

Elmore, S. (2007). Apoptosis: a Review of programmed cell death. Toxicol. Pathol. 35, 495–516.

Fabry, B., Maksym, G.N., Butler, J.P., Glogauer, M., Navajas, D., and Fredberg, J.J. (2001). Scaling the microrheology of living cells. Phys. Rev. Lett. 87, 148102.

Fernandes, P.A.L., Delcea, M., Skirtach, A.G., Möhwald, H., and Fery, A. (2010). Quantification of release from microcapsules upon mechanical deformation with AFM. Soft Matter 6, 1879–1883.

Fletcher, D.A., and Mullins, R.D. (2010). Cell mechanics and the cytoskeleton. Nature 463, 485–492.

Friedmann Angeli, J.P., Krysko, D.V., and Conrad, M. (2019). Ferroptosis at the crossroads of cancer-acquired drug resistance and immune evasion. Nat. Rev. Cancer 19, 405–414.

Galluzzi, L., and Vitale, I. (2018). Molecular mechanisms of cell death: recommendations of the nomenclature committee on cell death 2018. Cell Death Differ. 25, 486–541.

Galluzzi, L., Vitale, I., Aaronson, S.A., Abrams, J.M., Adam, D., Agostinis, P., Alnemri, E.S., Altucci, L., Amelio, I., Andrews, D.W., et al. (2018). Molecular mechanisms of cell death: recommendations of the nomenclature committee on cell death 2018. Cell Death Differ. 25, 486–541.

Hanahan, D., and Weinberg, R.A. (2000). The hallmarks of cancer review. Cell 100, 57–70.

Hessler, J.A., Budor, A., Putchakayala, K., Mecke, A., Rieger, D., Holl, M.M.B., Orr, B.G., Bielinska, A., Beals, J., and Baker, J. (2005). Atomic force microscopy study of early morphological changes during apoptosis. Langmuir 21, 9280–9286.

Humphreys, D.T., and Wilson, M.R. (1999). Modes of L929 cell death induced by TNF-α and other cytotoxic agents. Cytokine 11, 773–782.

Kaczmarek, A., Vandenabeele, P., and Krysko, D.V. (2013). Necroptosis: the release of damage-associated molecular patterns and its physiological relevance. Immunity 38, 209–223.

Kagan, V.E., Mao, G., Qu, F., Angeli, J.P.F., Doll, S., Croix, C.S., Dar, H.H., Liu, B., Tyurin, V.A., Ritov, V.B., et al. (2017). Oxidized arachidonic and adrenic PEs navigate cells to ferroptosis. Nat. Chem. Biol. 13, 81–90.

Kim, K.S., Cho, C.H., Park, E.K., Jung, M.H., Yoon, K.S., and Park, H.K. (2012). AFM-Detected apoptotic changes in morphology and biophysical property caused by paclitaxel in Ishikawa and HeLa cells. PLoS One 7, e30066.

Krysko, D.V., Vanden Berghe, T., D'Herde, K., and Vandenabeele, P. (2008). Apoptosis and necrosis: detection, discrimination and phagocytosis. Methods 44, 205–221.

Kwon, H.K., Lee, J.H., Shin, H.J., Kim, J.H., and Choi, S. (2015). Structural and functional analysis of cell adhesion and nuclear envelope nano-topography in cell death. Sci. Rep. 5, 1–15.

Liu, Y., Zhang, T., Zhou, Y., Li, J., Liang, X., Zhou, N., Lv, J., Xie, J., Cheng, F., Fang, Y., et al. (2019). Visualization of perforin/gasdermin/complement-formed pores in real cell membranes using atomic force microscopy. Cell. Mol. Immunol. 16, 611–620.

Marx, V. (2019). May mechanobiology work forcefully for you. Nat. Methods 16, 1083–1086.

Moreno-Gonzalez, G., Vandenabeele, P., and Krysko, D.V. (2016). Necroptosis: a novel cell death modality and its potential relevance for critical care medicine. Am. J. Respir. Crit. Care Med. 194, 415–428.

Nawaz, A.A., Urbanska, M., Herbig, M., Nötzel, M., Kräter, M., Rosendahl, P., Herold, C., Toepfner, N., Kubánková, M., Goswami, R., et al. (2020). Intelligent image-based deformation-assisted cell sorting with molecular specificity. Nat. Methods 17, 595–599.

Nikolaev, N.I., Mueller, T., Williams, D.J., and Liu, Y. (2014). Changes in the stiffness of human mesenchymal stem cells with the progress of cell death as measured by atomic force microscopy. J. Biomech. 47, 625–630.

Oropesa-Ávila, M., de la Cruz-Ojeda, P., Porcuna, J., Villanueva-Paz, M., Fernández-Vega, A., de la Mata, M., de Lavera, I., Rivero, J.M.S., Luzón–Hidalgo, R., Álvarez-Córdoba, M., et al. (2017). Two coffins and a funeral: early or late caspase activation determines two types of apoptosis induced by DNA damaging agents. Apoptosis 22, 421–436.

Pegoraro, A.F., Janmey, P., and Weitz, D.A. (2017). Mechanical properties of the cytoskeleton and cells. Cold Spring Harb. Perspect. Biol. 9, a022038.

Pelling, A.E., Veraitch, F.S., Chu, C.P.K., Mason, C., and Horton, M.A. (2009). Mechanical dynamics of single cells during early apoptosis. Cell Motil. Cytoskeleton 66, 409–422.

Purschke, M., Rubio, N., Held, K.D., and Redmond, R.W. (2010). Phototoxicity of Hoechst 33342 in time-lapse fluorescence microscopy. Photochem. Photobiol. Sci. 9, 1634–1639.

Rigato, A., Miyagi, A., Scheuring, S., and Rico, F. (2017). High-frequency microrheology reveals cytoskeleton dynamics in living cells. Nat. Phys. 13, 771–775.

Ros, U., Peña-Blanco, A., Hänggi, K., Kunzendorf, U., Krautwald, S., Wong, W.W.L., and García-Sáez, A.J. (2017). Necroptosis execution is mediated by plasma membrane nanopores independent of calcium. Cell Rep. 19, 175–187.

Segawa, K., and Nagata, S. (2015). An apoptotic 'eat me' signal: phosphatidylserine exposure. Trends Cell Biol. *25*, 639–650.

Silke, J., and Brink, R. (2010). Regulation of TNFRSF and innate immune signalling complexes by TRAFs and cIAPs. Cell Death Differ. *17*, 35–45.

Sokolov, I., Dokukin, M.E., Kalaparthi, V., Miljkovic, M., Wang, A., Seigne, J.D., Grivas, P., and Demidenko, E. (2018). Noninvasive diagnostic imaging using machine-learning analysis of nanoresolution images of cell surfaces: detection of bladder cancer. Proc. Natl. Acad. Sci. U S A *115*, 12920–12925.

Sollich, P., Lequeux, F., Hébraud, P., and Cates, M.E. (1997). Rheology of soft glassy materials. Phys. Rev. Lett. *78*, 2020–2023.

Su, X., Zhang, L., Kang, H., Zhang, B., Bao, G., and Wang, J. (2019). Mechanical, nanomorphological and biological reconstruction of early-stage apoptosis in HeLa cells induced by cytochalasin B. Oncol. Rep. *41*, 928–938.

Tang, D., Kang, R., Berghe, T. Vanden, Vandenabeele, P., and Kroemer, G. (2019). The molecular machinery of regulated cell death. Cell Res. *29*, 347–364.

Tyurina, Y.Y., St. Croix, C.M., Watkins, S.C., Watson, A.M., Epperly, M.W., Anthonymuthu, T.S., Kisin, E.R., Vlasova, I.I., Krysko, O., Krysko, D.V., et al. (2019). Redox (phospho)lipidomics of signaling in inflammation and programmed cell death. J. Leukoc. Biol. *106*, 57–81.

Vanhaesebroeck, B., Decoster, E., Van Ostade, X., Van Bladel, S., Lenaerts, A., Van Roy, F., and Fiers, W. (1992). Expression of an exogenous tumor necrosis factor (TNF) gene in TNF-sensitive cell lines confers resistance to TNF-mediated cell lysis. J. Immunol. *148*, 2785–2794.

Vercammen, D., Vandenabeele, P., Beyaert, R., Declercq, W., and Fiers, W. (1997). Tumour necrosis factor-induced necrosis versus anti-Fas-induced apoptosis in L929 cells. Cytokine *9*, 801–808.

Vercammen, D., Brouckaert, G., Denecker, G., Van De Craen, M., Declercq, W., Fiers, W., and

Vandenabeele, P. (1998). Dual signaling of the Fas receptor: initiation of both apoptotic and necrotic cell death pathways. J. Exp. Med. *188*, 919–930.

Weber, A., Iturri, J., Benitez, R., Zemljic-Jokhadar, S., and Toca-Herrera, J.L. (2019). Microtubule disruption changes endothelial cell mechanics and adhesion. Sci. Rep. *9*, 14903.

Wu, H.W., Kuhn, T., and Moy, V.T. (1998). Mechanical properties of L929 cells measured by atomic force microscopy: effects of anticytoskeletal drugs and membrane crosslinking. Scanning *20*, 389–397.

Xia, S., Lim, Y.B., Zhang, Z., Wang, Y., Zhang, S., Lim, C.T., Yim, E.K.F., and Kanchanawong, P. (2019). Nanoscale Architecture of the cortical actin cytoskeleton in embryonic stem cells. Cell Rep. *28*, 1251–1267.e7.

Zhang, Y., Chen, X., Gueydan, C., and Han, J. (2018). Plasma membrane changes during programmed cell deaths. Cell Res. *28*, 9–21.

Supplemental Information

AFM Analysis Enables Differentiation

between Apoptosis, Necroptosis,

and Ferroptosis in Murine Cancer Cells

Louis Van der Meeren, Joost Verduijn, Dmitri V. Krysko, and André G. Skirtach
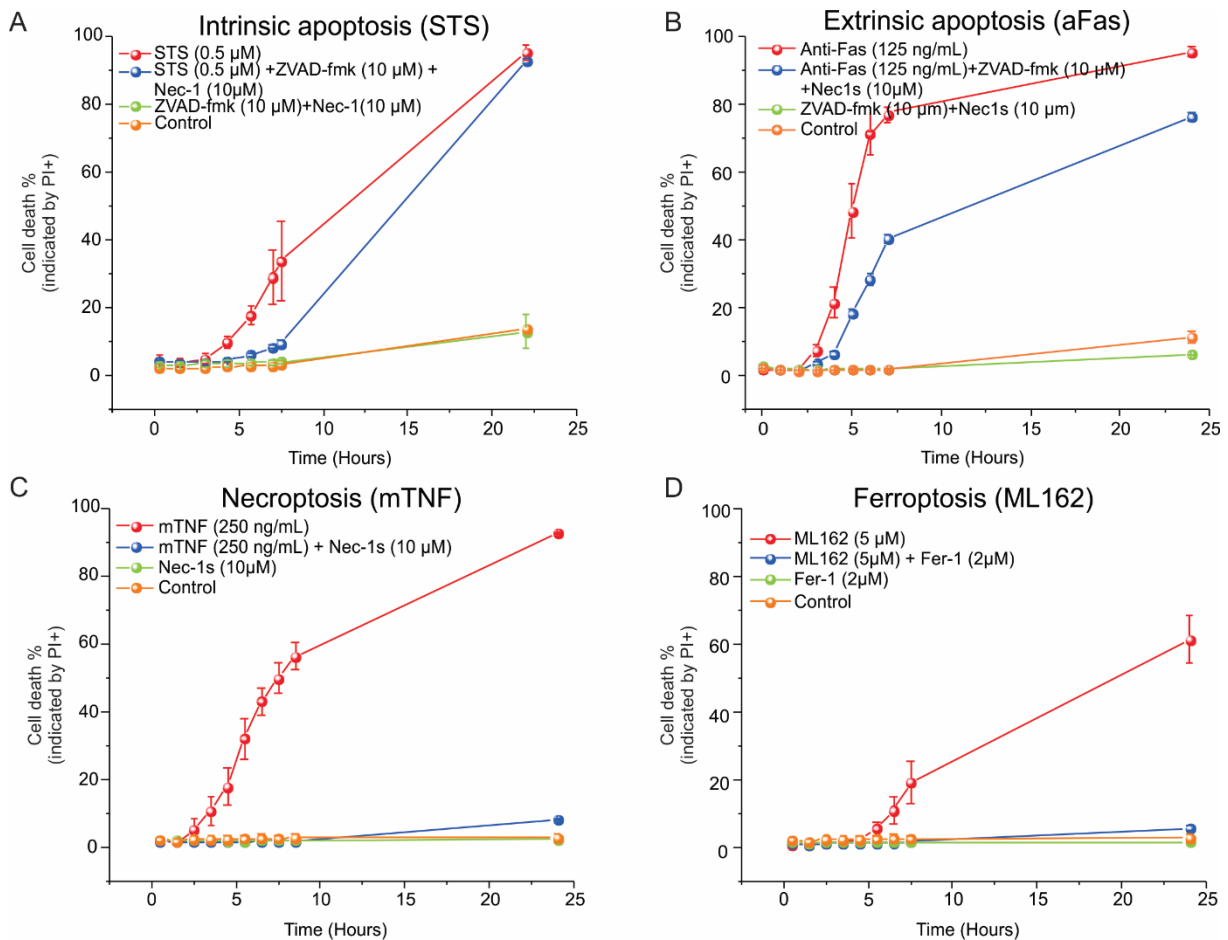
Figure S1 related to Figure 1 Cell death (RCD) time analysis of the induction/inhibition experiments to test if inducers stimulate the proclaimed cell death modality analyzed by wide-field fluorescence microscopy. The percentage of dead cells was calculated by counting the percentage of cells marked by Propidium Iodide (PI), which is a nuclear dye that can only enter cells after membrane permeabilization has occurred. By adding the specific inhibitor targeting a protein essential in initiating the respective process of regulated cell death (RCD), the cell death process can be inhibited or delayed. In the performed experiments, all inhibitors were added 30 minutes before cell death inducers. (**A**) The addition of pan-caspase inhibitor zVAD-fmk delays extrinsic apoptotic cell death after the induction with STS by inhibiting caspase activation, however, a complete inhibition is not possible since caspase inhibition eventually leads to cell death as was proven in previous research(Wu et al., 2011). (**B**) zVAD-fmk addition leads to a delay of intrinsic apoptosis after the induction with Anti-Fas antibody, by inhibiting caspases. However, similar to the observation in extrinsic apoptosis no complete inhibition is possible due to the occurrence of zVAD-fmk induced necroptosis. (**C**) Necrostatin-1s inhibits RIPK1 activation, which essential in the execution of necroptosis. Here the addition of Nec1s successfully inhibits necroptotic cell death after induction with mTNF (Takahashi et al., 2012). (**D**) Ferrostatin-1 is a lipid-ROS scavenger that allows inhibiting ferroptotic cell death by targeting lipid ROS produced after the addition of ML162 (Dixon et al., 2012). In the performed experiments, it is observed that ferroptosis was effectively inhibited by adding Fer-1.
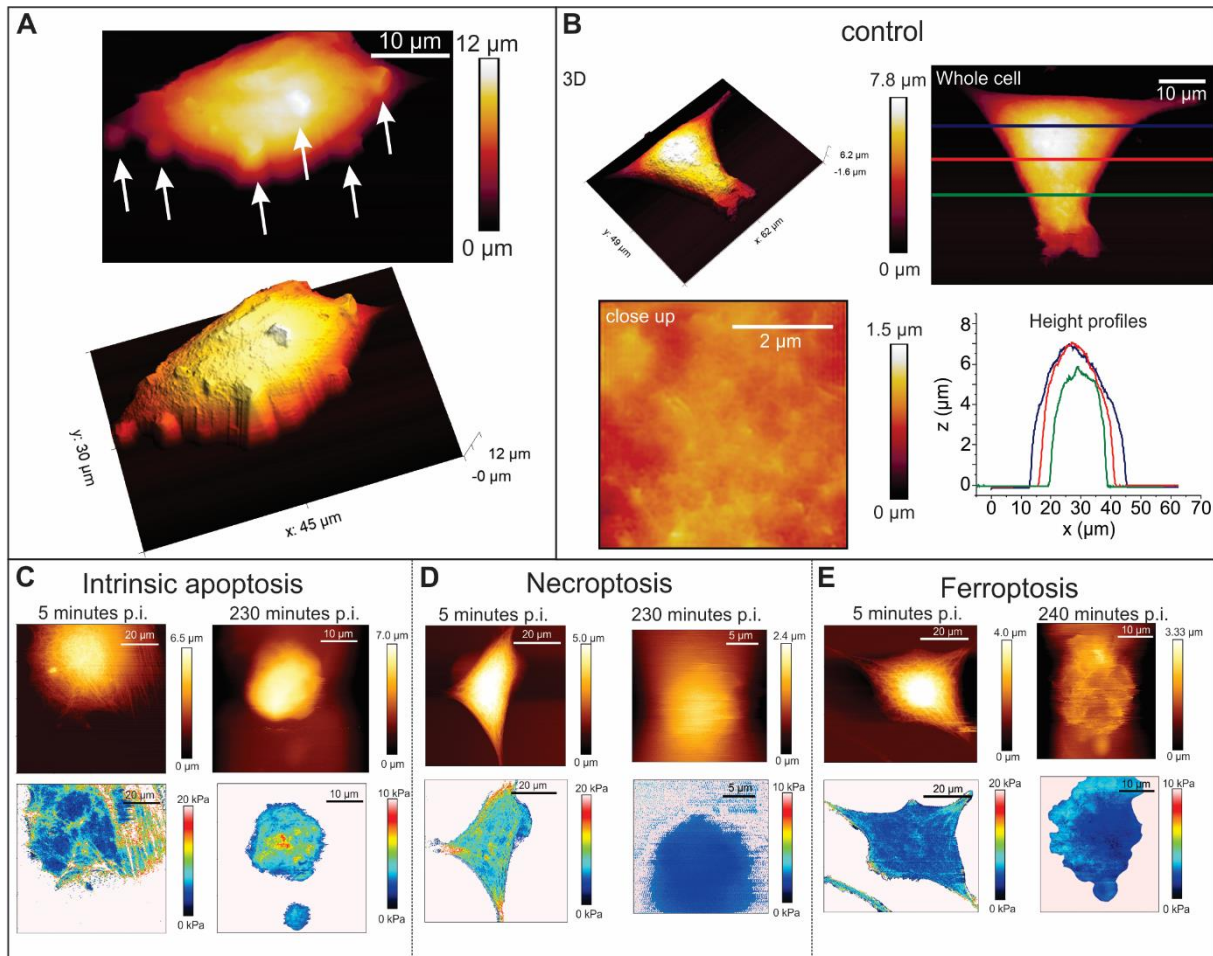
Figure S2 related to Figure 2 Morphological AFM analysis of control cells.
(**A**) Top: 3D (left) and 2D (right) of a control. Bottom left: control cells, imaged with confocal microscopy, exhibit the typical morphology of live L929sAhFas cells (blue stain: Hoechst33342 DNA stain). Bottom right: close up of the membrane of a control cell that shows a smooth membrane surface without any remarkable disruptions. (**B**) Additional height image (2D and 3D) showing the typical morphology of a ferroptotic cell. White arrows: circular protrusions originating from the cellular membrane that were frequently observed after induction of ferroptotic cell death. (**C-E**) Example of live imaging of cells during the process of RCD (Left to right: Intrinsic apoptosis, necroptosis, and ferroptosis). Top row: height image, Bottom row: pixel-by-pixel Young's modulus mapping.
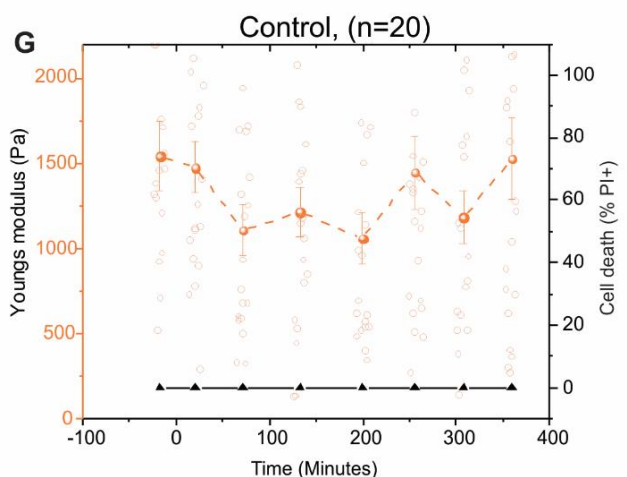
A

	0H post induction	2H post induction	6H post induction
Intrinsic apoptosis (STS)			
Extrinsic apoptosis (aFas Ab)			
Necroptosis (mTNF)			
Ferroptosis (ML162)			

B Control

C Rate of elasticity change

D Extrinsic apoptosis (STS)

E Intrinsic apoptosis (aFas)

F Ferroptosis (ML162), (n=20)

G Control, (n=20)
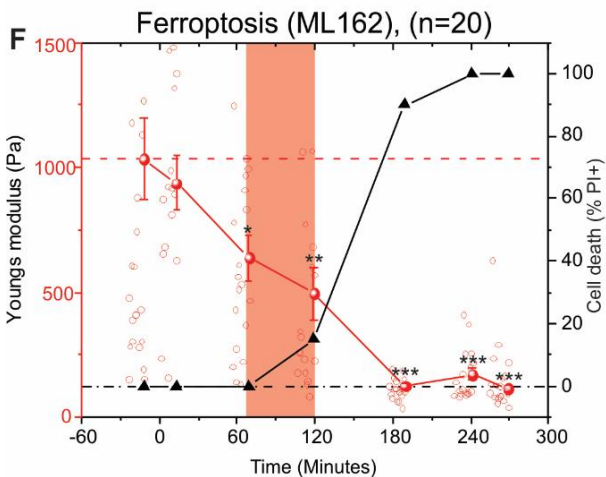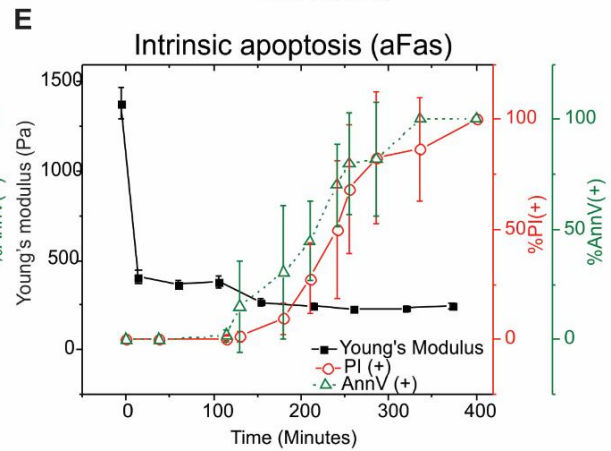
Figure S3 related to Figure 3. Fluorescence microscopy analysis of RCD.

(**A**) (i.e. membrane permeabilization, PI$^+$) was during AFM (Scale bar = 20 μm). (**B**) Dynamics of the mechanical p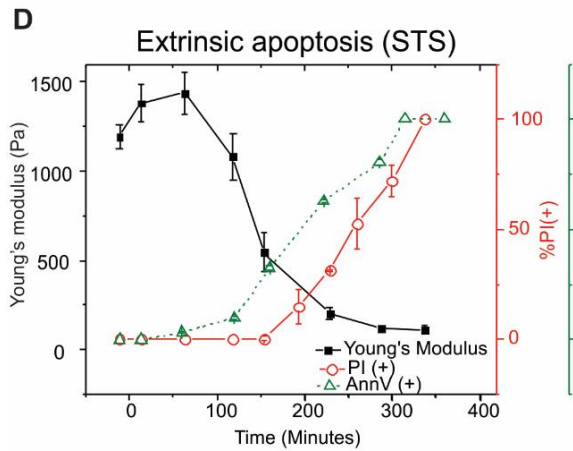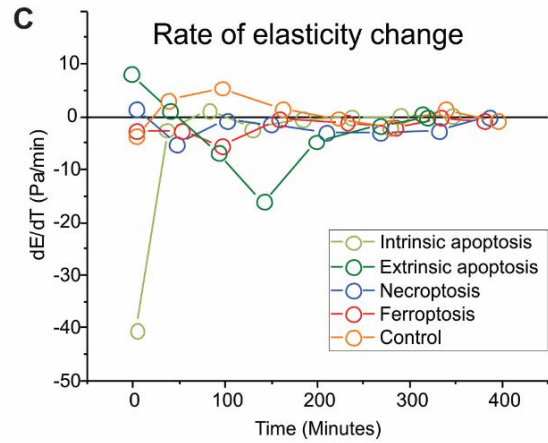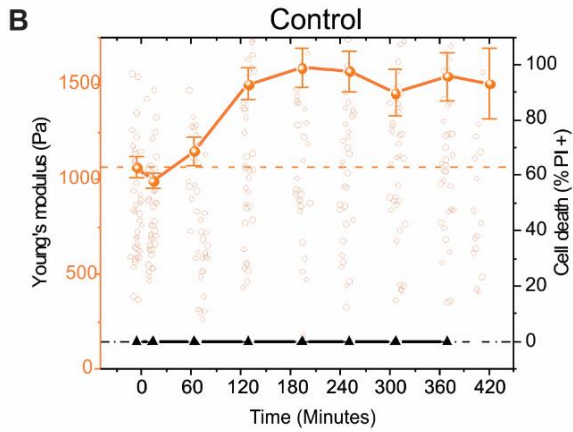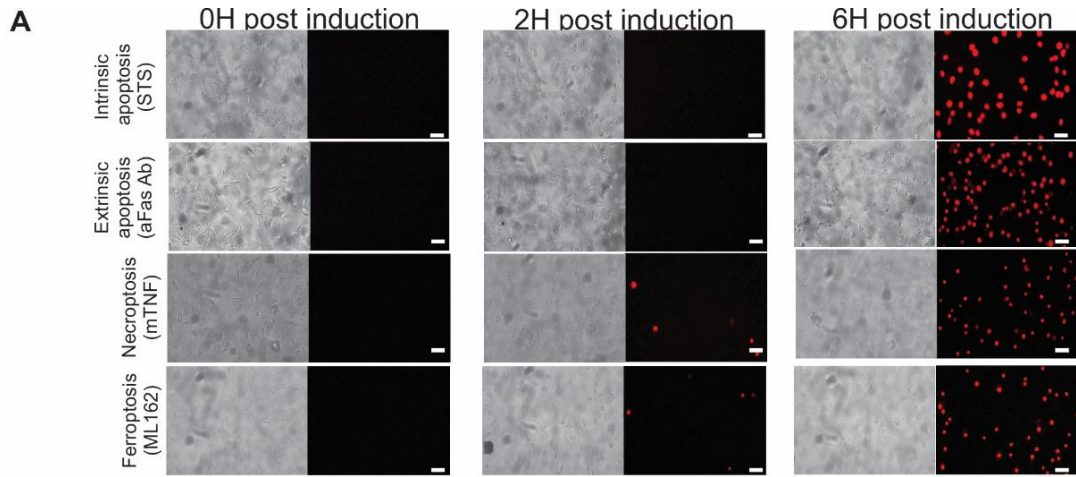roperties in the control cells. The left Y-axis indicates elasticity, right Y-axis cell death as measured by the percentage of PI$^+$ cells. Error bars indicate the standard error of means (SEM). An increase can be noticed in elasticity during the initial timepoints of the experiments that can be noticed. This is most likely caused by suboptimal conditions during the transferring samples; however, this is stabilized during the later stages of the experiments. (**C**) Comparison of the rates of elasticity changes during the process of RCD (obtained by taking the first-order derivative of the elasticity during the process of cell death for each of the investigated modality). Lower values indicate faster decrease rates. (**D-E**) Time dependence of the elasticity experiments superimposed on fluorescence measurements combining both Propidium iodide and Annexin V labels to indicate the late and early cell death, respectively in (**D**) extrinsic apoptosis and (**E**) intrinsic apoptosis. (**F**) Dynamics of cellular elasticity during ferroptosis, measured in an MCA205 cell line. A colored rectangle indicates the delay between the first significant decrease of cellular elasticity and the first signal of cell death (PI$^+$). Significance was calculated using the Wilcoxon rank-sum test (*p <0.05, **p<0.01, ***p<0.001, error bars indicate SEM). (**G**) dynamics of cellular elasticity in the control MCA205 cells.
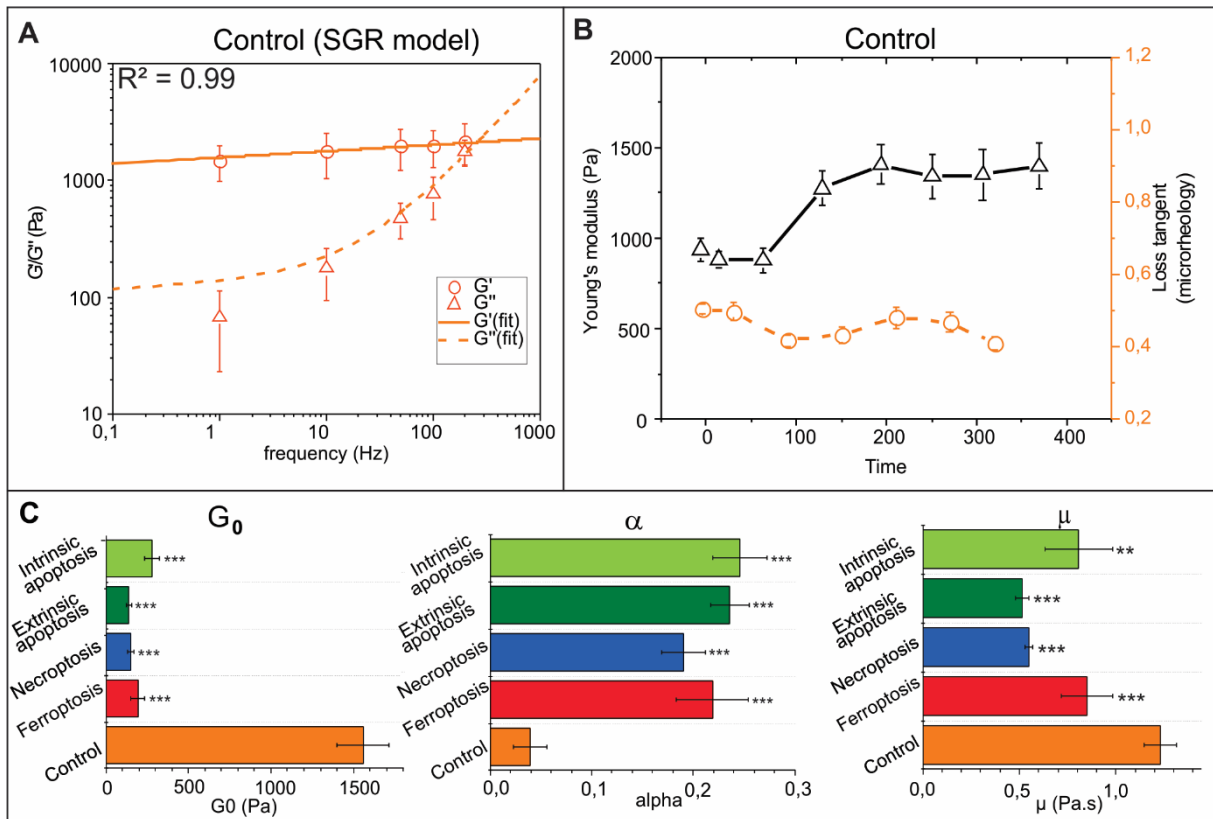
Figure S4 related to Figure 4. Microrheological analysis of RCD.

(**A**) SGR model fit over a frequency range from 1 to 200 Hz in control cells, G' indicates shear storage and G''
indicates shear loss. The points indicate points obtained by measurements while the lines refer to the values of
the fitted models, R^2 value in the top left corner indicates the correlation of the measured data with the proposed
SGR model, this high correlation allows to use the interpretation of this model for further analysis. Error bars
show standard deviation (n=10). (**B**) A pairwise comparison of elasticity versus dynamic in cellular microrheology
(represented by a loss tangent) the loss tangent remains stable throughout the experiment. The error bars in the
loss tangent graphs indicate the standard error of means (SEM) n=30. (**C**) Bar graphs comparing the parameters
resulting from the SGR models, G_0 scaling factor (Pa), alpha: power-law exponent, μ: Newtonian viscosity factor
(Pa/s) (detailed explanation of these parameters can be found in Supplementary notes 2). Error bars indicate
standard deviation (n=5), significance was calculated using a two-sample Student's t-test (**p<0.01,
***p<0.001).

Table S1 related to Figure 3. Statistical comparison of the time delay between AFM detection and the appearance of the first fluorescent signal. The onset of RCD onset detection with AFM compared to PI+ signal, (statistical significance is compared to control cells ***p<0.001, p-values were obtained using a Wilcoxon rank-sum test).

RCD	First significant elasticity decrease (minutes post induction)	p-value (vs. Control)	First increase PI+ signal (minutes post-induction)	Δt (min)
Intrinsic apoptosis	14	7.85E-15 ***	180	**166**
Extrinsic apoptosis	153	7.18E-08 ***	193	**40**
Necroptosis	83	7.80E-04 ***	182	**99**
Ferroptosis	81	2.07E-05 ***	236	**155**

Table S2 related to Figure 3. Rate of elasticity change per measured time point. Numerical data used to visualize the graph shown in Figure S1C

Intrinsic apoptosis		Extrinsic apoptosis		Necroptosis		Ferroptosis	
Time (minutes)	dE/dt (Pa/min)	Time (minutes)	dE/dt (Pa/min)	Time (minutes)	dE/dt (Pa/min)	Time (minutes)	dE/dt (Pa/min)
4	-40.35963	1	14.52216	2.5	1.57944	3.5	-2.68251
36.75	-2.52451	38.5	-2.46024	47.5	-5.13107	52	-2.66814
82.5	1.26965	91	-6.13272	102	-0.64558	97	-5.52833
129.75	-2.24311	136	-14.76087	149	-1.44514	158	-0.41409
183.75	-0.33762	173.5	-4.94972	208.5	-3.05878	232	-1.14444
237	-0.2579	211	-4.37092	268	-3.1066	283.5	-1.94438
290.25	0.04891	258	-1.78066	331.5	-2.54441	333.25	-0.2535
346.25	0.10415	312.5	0.36987	386	-0.04629	380	-0.77324

Table S3 related to Figure 3. Statistical analysis of the rate of the elasticity change. Significance test for the rate of elasticity decrease in each of the RCD modalities, (***p<0.001, p-values were calculated using a two-sample Student's t-test).

RCD	Max rate of elasticity change (Pa/min)	Sd (±)	Vs. intrinsic apoptosis	Vs. extrinsic apoptosis	Vs. necroptosis	Vs. ferroptosis
Intrinsic apoptosis	**-42.27**	**26.97**	1	3.04e-7 ***	4.01e-13 ***	9.79e-14 ***
Extrinsic apoptosis	**-16.21**	**14.58**	3.04e-7 ***	1	3.75e-5 ***	3.79e-6 ***
Necroptosis	**-5.13**	**7.46**	4.01e-13 ***	3.75e-5 ***	1	0.27
Ferroptosis	**-3.57**	**6.07**	9.79e-14 ***	3.79e-6 ***	0.27	1

Table S4 related to figure 4 Statistical comparison of the delay between elasticity and microrheology changes during RCD modalities. Overview table comparing the delay between a significant change in elasticity versus significant change` in loss tangent for each of the regulated cell death modalities (statistical significance is compared to control cells * p <0.05, ** p<0.01, *** p<0.001).

RCD	First significant loss tangent increase (minutes post-induction)	p-value (vs. Control)	First significant elasticity decrease (minutes post-induction)	Δt (min)
Intrinsic apoptosis	37.5	2.85E-10 ***	14	**23.5**
Extrinsic apoptosis	163.5	6.11E-03 **	153	**9.5**
Necroptosis	259	4.67E-03 **	83	**176**
Ferroptosis	253	4.77E-04 ***	81	**172**

Transparent methods:

Cell culture and regulated cell death induction: L929sAhFAS fibrosarcoma cells were cultured in Dulbecco's Modified Eagle Medium (LONZA, 12-604F) supplemented with 10% FBS (FisherScientific, 11591821), 1% Penicillin/streptomycin (LONZA, DE17-602E) (Vanhaesebroeck et al., 1992; Vercammen et al., 1997). Different modes of cell death were induced by adding the corresponding compounds. MCA205 cells were cultured in RPMI 1640 (LONZA, BE12-702F) supplemented with 10% FBS (FisherScientific, 11591821), 1% Penicillin/streptomycin (LONZA, DE17-602E). Extrinsic apoptosis is induced by STS (VWR, 569396-100, 1 µM), intrinsic apoptosis is induced by adding aFas antibody (Merck, 05-201, 125 ng/mL), necroptosis is induced by adding mTNF-alpha (recombinant protein from VIB Protein Service Facility, 250 ng/mL) and ferroptosis is induced by adding ML162 (SanBio, 20455-5, 10 µM). Induction of ferroptosis in MCA205 cells is induced equally as in L929sAhFas cells by adding ML162.

Cell death type confirmation experiments: For the cell death induction experiment (Figure 1S), cells were seeded in a 96 well plate (VWR, 10062-900) to a density of 10000 cells per well one day prior. To visualize the state of cells two stains were added: propidium iodide (1µg/mL; Thermofisher, P1304MP), and Hoechst33342 (1µg/mL; Thermofisher, 62249). Inhibitors were added 30 minutes before the cell death inducers (zVAD-fmk, Nec1s, and Fer1 for apoptosis, necroptosis, and ferroptosis respectively). Once inducers are added (concentrations are indicated in Figure S1), imaging is initiated. Images are made with a Nikon Ti eclipse every hour. Cell death was assessed by overlapping Hoechst 33342 (live) stain and propidium iodide (death, membrane-impermeable) stain in FIJI. During imaging, the cells are incubated at 37°C with 5% CO2.

High-resolution optical images were made on a Nikon confocal scanning laser microscope (Figure 1), in these experiments three fluorescent labels were used namely: Hoechst 33342 (DNA stain live cells, blue) (Thermofisher, 62249), Alexa fluor 488 Annexin V (phosphatidylserine exposure stain, green) (Thermofisher, A13201) and propidium iodide (DNA stain dead cells, red) (Thermofisher, P1304MP). During these experiments, cells were imaged at different time points after induction.

AFM morphological analysis: For all AFM experiments cells were seeded 1 day before the experiments on glass-bottom Petri dishes (confocal dishes) to a concentration of 55.000 cells mL^{-1}. Topographical images were acquired using the nanowizard 4™ (JPK GmbH Instruments/Bruker) in the JPK QI® mode using ATEC-CONT cantilevers, these sharp tip cantilevers (radius of curvature < 10 nm) have an increased tip height (15 µm) to avoid contact of the cantilever and the cells during imaging. Before topographical imaging, the cells were fixed at 3 hours post-induction. This time point was determined based on CLSM images. First, the dishes were washed 3 times with PBS, consequently, a 4% Paraformaldehyde (PFA, Alfa Aesar™, 043368.9M) solution was added for 10 minutes finally the PFA solution was replaced with PBS, and in-between measurements, cells were stored at 4°C For each RCD modalities 3 areas of 5 by 5 µm were analyzed on 5 different cells (n=15 total). Based on this data the average roughness (Ra), root means square roughness (Rq), and the peak-to-valley roughness (Rt) was calculated for each RCD modality. Significance compared to control was analyzed using a two-sample Student's t-test, since the roughness data have a normal distribution.

AFM elasticity analysis: For all AFM experiments, cells were seeded 24 hours before the experiments on glass-bottom Petri dishes, treated for increased attachment (VWR, 75856-740), to a concentration of 55.000 cells/mL. The AFM instrument used during all experiments is the nanowizard 4™ with a manual stage (JPK GmbH Instruments/Bruker). To ensure optimal conditions during the live-cell mechanical measurements an incubator was constructed around the AFM instrument allowing control of temperature and CO_2 (37°C and 5% CO_2), all force curves were acquired in contact mode using a colloidal probe, containing a spherical tip of 5 µm diameter (CP-qp-SCONT-BSG, force constant 0.1 N m^{-1}) and using a setpoint of 2 nN at 2 µm/s. Elasticity measurements were performed 5 minutes before and 15 minutes after adding the cell death inducer. The time at which the inducer is added is set as 0 minutes (which means the first measurement occurs at approximately -5 minutes). After the initial points, every 30 minutes measurements were performed. These measurements were continued until the end stage of cell death was reached for all cells in the experiments as was indicated by PI positivity (at later timepoints cells were detached and flow away rendering localization impossible). At each time point, three consecutive force curves were collected from 50 cells divided over 3 experiments (measurements were aimed above the nucleus). Simultaneously with the AFM measurements fluorescent markers added to verify cellular status, here PI was

used to indicate a late stage of cell death. To obtain Young's modulus from the force curves a Hertz model adjusted for spherical indenters is used (equation 1, using a Poisson ratio of 0.5), in the JPK data processing software (JPK, Germany; Butt et al., 2005). Young's modulus calculations were based on 400 nm indentation assuming an average cell height of 5 μm which increases as cells start to swell up and detach. (<10% of the maximum cellular height).

$$F = \frac{E}{1 - \nu} \left[\frac{a^2 + R^2}{2} \ln\left(\frac{R + a}{R - a}\right) - aR \right] \ (equation\ 1)$$

$$(R = radius\ of\ the\ sphere, a = radius\ of\ contact\ circle)$$

$$\delta = \frac{a}{2} \ln\left(\frac{R + a}{R - a}\right)$$

$$(\delta = indentation\ depth = vertical\ tip\ position)$$

Elasticity experiments on MCA205 cells were performed identically as for the L929sAhFas cells, here 20 cells were analyzed over 2 experiments.

AFM microrheology measurements: To gain information on the viscoelastic properties of cells, microrheological measurements were performed. In these measurements, the force reaction toward small amplitude oscillating forces (at low frequencies) that are applied at the membrane are analyzed. For these measurements, qp-BIO-AC chips were used and more specifically the CB3 cantilever, with a 30 nm tip (force constant = 0.06 N m^{-1}). An initial set-point of 400 pN was chosen to approach the cells, during the oscillations in the experiments were performed with an amplitude of 20 nm at frequencies ranging between 1 and 100 Hz (20 oscillation cycles). To follow the loss tangent dynamics over time, three consecutive microrheology measurements were performed on a total of 30 cells at each time point, at the frequency of 100Hz for 20 cycles (10 cells per experiment). Calculations of the storage and the loss moduli were performed in JPK data processing software, based on calculations adapted from a previous paper on microrheological measurements on live cells(Alcaraz et al., 2003). To accommodate for influences originating from the cantilever's geometry, first, the deviation from the 90° phase shift in a liquid environment and the hydrodynamic drag coefficient was calculated and incorporated into the measurements (*PZT-lag = 5.4°, b(h$_0$)= 3.3e-6*). Fitting the microrheological data to the soft glassy rheology model was performed by non-linear fitting in OriginPRO 2020.

A common way to determine the microrheological properties of soft materials is by determining the shear modulus (G*(w)). This data can be obtained by performing oscillation experiments on the surface of the material and determining the complex ratio between the applied stress and the resulting strain. The shear modulus can be split into a real and an imaginary part which represents respectively the stored energy (G') and the energy dissipated inside the material (G''), these values can be calculated using Equation 2. The ratio between these two parts (G''/G', also referred to as the loss tangent) relates to how a material leans more towards a liquid- or solid-like mechanical behavior (Alcaraz et al., 2003). From a multitude of different microrheological researches, it seemed that the soft glassy rheological model is a very useful model to understand the cytoskeletal rheology, this model, the equation for this model is shown in equation S2(Kollmannsberger and Fabry, 2009). To take into account, the phase shift due to drag between the cantilever and the liquid, the piezo-lag, and the hydrodynamic drag ($b(h_0)$) are calculated (Supplemental Figure N2).

$$G^*(\omega) = G'(\omega) + iG''(\omega) = \frac{1-\nu}{3\delta_0 \tan(\theta)} \left(\frac{F(\omega)}{\delta(\omega)} - i\omega b(h_0) \right) \text{ (Equation 2)}$$

$$G^* = G_0 \left(1 + i \, tan \left(\theta \cdot \frac{\pi}{2} \right) \right) (\omega)^\alpha + i\mu\omega \text{ (Equation 3)}$$

G_0: scaling factor (Pa), α: power-law exponent, μ: Newtonian viscosity value (Pa.s), ϑ: phase shift, $b(h_0)$: hydrodynamic drag coefficient, ω: oscillation frequency, F(ω): measured deflection, δ(ω): measured height.

Fabry *et al.* suggested (Fabry et al., 2001) a physical interpretation of the power-law behavior of cells in microrheological measurements in a specific case of soft glassy materials. This interpretation represents the cytoskeleton as a glassy material, made up of structural elements in a matrix i.e. the cytoskeleton that can both interact and bind with each other (solid-like behavior) but also can reorganize and flow independently (fluid-like behavior). The soft glassy rheology model (SGR) provides three parameters namely: G0, α, and μ (Figures 2B, Figure S2A, Figure S2C; Alcaraz et al., 2003). The significantly decreased value for G0, a measure of the elasticity at the glass transition, for all RCD modalities logically supports the conclusions of the elasticity analysis. The parameter α is a measure for matrix agitation or how much the cytoskeleton differs from glass transition, i.e. solid state. This value can range from

0 (solid) to 1 (liquid). The increased value for α depicts a decrease in the interaction between the matrix components. This observation, together with the decreased value for μ, is a measure for the Newtonian viscosity indicating that at the late stages of RCD the cytoskeleton has lost most of its interactions between matrix components (solid behavior) and is more freely flowing (fluid behavior).

Cytoskeleton immunofluorescence imaging: Cells were seeded onto poly-L-lysine (Merck, A-005-C) coated coverslips (18mm, VWR, 48380-046) in a concentration of 60 000 cells mL^{-1}. One day after seeding, inducers were added in concentrations as mentioned above. At chosen time points cells were washed 3 times with PBS and consequently fixed using 4% PFA (Alfa Aesar™, 043368.9M) for 10 minutes. Cells are then permeabilized using Triton X-100. A blocking step using 2% BSA was done overnight at 4°C. Next, the cells were incubated for 3 hours with the primary antibody in a concentration of 2 µg mL^{-1} (alpha Tubulin Monoclonal Antibody (DM1A), Thermofisher, 62204). As a next step cells were incubated in a staining medium for 45 minutes which contained: Hoechst33342 (1 µg mL^{-1}), ActinRed™ 555 ReadyProbes (Thermofisher, R37112) and Goat anti-Mouse IgG (H+L) Highly Cross-Adsorbed Secondary Antibody, Alexa Fluor 488 (1 µg mL^{-1}) (Thermofisher, A-11029). Finally, after washing, the coverslips were mounted using SlowFade™ Glass Soft-set Antifade Mountant (Thermofisher, S36917).

Statistical analysis: All statistical analysis is performed in the software package RStudio. To analyze the difference in morphological roughness between different cell death modalities and control cells, a Kruskal-Wallis test was performed followed by a pairwise Wilcoxon test with Benjamini-Hochberg adjusted p-values. To compare the elasticity at different time points during the RCD process against the values for control cells, a Wilcoxon-rank sum test is used. The difference in the rate of elasticity change between RCD modalities was analyzed with a Kruskal-Wallis test followed by a pairwise Wilcoxon test with Benjamini-Hochberg adjusted p-values. The values of the loss tangent during the process of RCD were compared to those of control cells using a Wilcoxon-rank sum test at each time point.

Supplemental references:

Alcaraz, J., Buscemi, L., Grabulosa, M., Trepat, X., Fabry, B., Farré, R., and Navajas, D. (2003). Microrheology of human lung epithelial cells measured by atomic force microscopy. Biophys. J. *84*, 2071–2079.

Butt, H.J., Cappella, B., and Kappl, M. (2005). Force measurements with the atomic force microscope: Technique, interpretation and applications. Surf. Sci. Rep. *59*, 1–152.

Dixon, S.J., Lemberg, K.M., Lamprecht, M.R., Skouta, R., Zaitsev, E.M., Gleason, C.E., Patel, D.N., Bauer, A.J., Cantley, A.M., Yang, W.S., et al. (2012). Ferroptosis: An iron-dependent form of nonapoptotic cell death. Cell *149*, 1060–1072.

Fabry, B., Maksym, G.N., Butler, J.P., Glogauer, M., Navajas, D., and Fredberg, J.J. (2001). Scaling the microrheology of living cells. Phys. Rev. Lett. *87*.

Kollmannsberger, P., and Fabry, B. (2009). Active soft glassy rheology of adherent cells. Soft Matter *5*, 1771.

Takahashi, N., Duprez, L., Grootjans, S., Cauwels, A., Nerinckx, W., Duhadaway, J.B., Goossens, V., Roelandt, R., Van Hauwermeiren, F., Libert, C., et al. (2012). Necrostatin-1 analogues: Critical issues on the specificity, activity and in vivo use in experimental disease models. Cell Death Dis. *3*, e437-10.

Vanhaesebroeck, B., Decoster, E., Van Ostade, X., Van Bladel, S., Lenaerts, A., Van Roy, F., and Fiers, W. (1992). Expression of an exogenous tumor necrosis factor (TNF) gene in TNF-sensitive cell lines confers resistance to TNF-mediated cell lysis. J. Immunol. *148*.

Vercammen, D., Vandenabeele, P., Beyaert, R., Declercq, W., and Fiers, W. (1997). Tumour necrosis factor-induced necrosis versus anti-Fas-induced apoptosis in L929 cells. Cytokine *9*, 801–808.

Wu, Y.T., Tan, H.L., Huang, Q., Sun, X.J., Zhu, X., and Shen, H.M. (2011). ZVAD-induced necroptosis in L929 cells depends on autocrine production of TNFα mediated by the PKC-MAPKs-AP-1 pathway. Cell Death Differ. *18*, 26–37.